Bioactive Materials 6 (2021) 2452–2466

Contents lists available at ScienceDirect

Bioactive Materials

journal homepage: www.sciencedirect.com/journal/bioactive-materials

Hypoxia response element-directed expression of bFGF in dental pulp stem cells improve the hypoxic environment by targeting pericytes in SCI rats

Sipin Zhu [a,1], Yibo Ying [a,1], Yan He [e,1], Xingxing Zhong [f], Jiahui Ye [a], Zhiyang Huang [a], Min Chen [a], Qiuji Wu [a], Yifan Zhang [a], Ziyue Xiang [a], Yurong Tu [a], Weiyang Ying [c], Jian Xiao [b,h], Xiaokun Li [b,h,***], Qingsong Ye [d,g,i,**], Zhouguang Wang [a,b,*]

[a] Department of Orthopaedics, The Second Affiliated Hospital and Yuying Children's Hospital of Wenzhou Medical University, Wenzhou, Zhejiang, 325000, China
[b] Molecular Pharmacology Research Center, School of Pharmaceutical Science, Wenzhou Medical University, Wenzhou, Zhejiang, China
[c] Department of Pain Medicine, The Second Affiliated Hospital and Yuying Children's Hospital of Wenzhou Medical University, Wenzhou, 325000, Zhejiang, China
[d] School and Hospital of Stomatology, Wenzhou Medical University, Wenzhou, 325035, China
[e] Laboratory of Regenerative Medicine, Tianyou Hospital, Wuhan University of Science and Technology, Wuhan, 430064, China
[f] The Department of Cardiology, The First Affiliated Hospital, School of Medicine, Zhejiang University, China
[g] Massachusetts General Hospital, Harvard University, Boston, 02114, USA
[h] Research Units of Clinical Translation of Cell Growth Factors and Diseases Research, Chinese Academy of Medical Science, China
[i] Center of Regenerative Medicine, Renmin Hospital of Wuhan University, Wuhan, 630060, China

ARTICLE INFO

Keywords:
Spinal cord injury
Adeno-associated virus
Basic fibroblast growth factor
Dental pulp stem cell
Vascular regulation
Hypoxic microenvironment

ABSTRACT

Cell-based transplantation strategies possess great potential for spinal cord injury (SCI) repair. Basic fibroblast growth factor (bFGF) has been reported to have multiple neuro-promoting effects on developing and adult nervous system of mammals and considered a promising therapy for nerve injury following SCI. Human dental pulp stem cells (DPSCs) are abundant stem cells with low immune rejection, which can be considered for cell replacement therapy. The purpose of this study was to investigate the roles of DPSCs which express bFGF under the regulation of five hypoxia-responsive elements (5HRE) using an adeno-associated virus (AAV-5HRE-bFGF-DPSCs) in SCI repairing model. In this study, DPSCs were revealed to differentiate into $CD13^+$ pericytes and up-regulate N-cadherin expression to promote the re-attachment of $CD13^+$ pericytes to vascular endothelial cells. The re-attachment of $CD13^+$ pericytes to vascular endothelial cells subsequently increased the flow rate of blood in microvessels via the contraction of protuberance. As a result, increased numbers of red blood cells carried more oxygen to the damaged area and the local hypoxia microenvironment in SCI was improved. Thus, this study represents a step forward towards the potential use of AAV-5HRE-bFGF-DPSCs in SCI treatment in clinic.

1. Introduction

Spinal cord injury (SCI) is a devastating event that leads to long-lasting neurological deficits manifested by motor, sensory and autonomic dysfunctions below the level of injury [1,2]. Conventional researches have suggested that the vessel rupture after SCI causes inflammation including ischemia, vasospasm and substantial internal bleeding [3–6]. At the same time, neurons that require high oxygen demand die due to insufficient blood perfusion [7–9]. Recent studies of Zhou et al. has demonstrated that microvessels are present in injured area as early as three days after injury, then the microvessel density increases up to 540% during the chronic phase of SCI [7,10,11]. However, the hypoxic microenvironment caused by SCI are not improved after microvessel regeneration [12]. Therefore, investigating factors that can alleviate central hypoxia in SCI is one of the key targets in the treatment of SCI [13–15].

Peer review under responsibility of KeAi Communications Co., Ltd.
* Corresponding author. Department of Orthopaedics, The Second Affiliated Hospital and Yuying Children's Hospital of Wenzhou Medical University, Wenzhou, Zhejiang, 325000 China.
** Corresponding author. School and Hospital of Stomatology, Wenzhou Medical University, Wenzhou 325035, China.
*** Corresponding author. Research Units of Clinical Translation of Cell Growth Factors and Diseases Research, Chinese Academy of Medical Science, China.
E-mail addresses: lixk1964@163.com (X. Li), qingsongye@hotmail.com (Q. Ye), wzhouguang@gmail.com (Z. Wang).
[1] These authors contributed equally to this work.

https://doi.org/10.1016/j.bioactmat.2021.01.024
Received 7 December 2020; Received in revised form 7 January 2021; Accepted 19 January 2021

Due to the non-reproducibility of central neurons, physical therapy, drug therapy, rehabilitation therapy and other treatments have little efficacy on recovering functions of injured nerves [16,17]. Accumulating evidences have suggested stem cells transplantation as a potential therapeutic for SCI [18,19]. However, stem cell transplantation faces various challenges including ethical issues of cell sources and immune rejection in clinical trials [20]. Here, we selected dental pulp stem cells (DPSCs) as the source of transplanted cells. DPSCs are highly proliferated and multilineage-differentiated thus can be used as autologous transplants. In addition, DPSCs can be easily isolated from freshly extracted teeth without causing adverse health effects [21,22]. Their convenience of isolation, lack of ethical controversy and low immunogenicity make DPSCs widely used in clinic [23,24]. DPSCs are characterized to be highly clonogenic with multi differentiation and neurovascular properties. Under specific condition, DPSCs could differentiate into mature neuronal cells both *in vitro* and *in vivo* [25]. DPSCs have been shown to hold tremendous regenerative potential in damaged central nervous system and be more potent than bone marrow mesenchymal stem cells at promoting functional recovery after SCI [26,27]. Hence, DPSCs are a promising candidate for transplantation therapy of SCI. bFGF has been considered a candidate molecule for SCI repair [28]. Previous researches have shown that bFGF plays significant roles in growth and development of nervous system [29]. However, the therapeutic effect was not achieved when bFGF was applied into SCI site using common delivery methods [30]. The possible reason might be that the transplanted stem cells are difficult to survive in SCI microenvironment, which results in the failure of bFGF to mediate SCI repair via promoting proliferation and differentiation of stem cells [8,29,31]. Thus, improving the ischemic and hypoxic microenvironment after SCI and combining bFGF with transplanted DPSCs for repairing SCI have become primary aims of our research.

In this study, we employed hypoxia-response element (HRE) to mediate the expression of human bFGF with adeno-associated virus (AAV) used as the vector, which potentially paves the way for future clinical trials [32,33]. To this end, AAV-5HRE-bFGF-DPSCs were generated and transplanted to the injured site of SCI. To investigate the mitigating factors of hypoxic environment, the expression of blood-vessel associated proteins including N-cadherin, alanyl aminopeptidase (CD13), beta platelet derived growth factor receptor (PDGFR-β) and platelet endothelial cell adhesion molecule (CD31) were examined. Hypoxia inducible factor 1 alpha (HIF-1α) was used as an indicator to observe the change of hypoxia. At the same time, the restoration of neural function was investigated by assessing the number of neurons and the regeneration of axons, which was indicated by neuronal nuclei protein (NeuN), neuromodulin (GAP43) and neurofilament protein (NF200). The roles of AAV-5HRE-bFGF-DPSCs in recovering motor function in SCI rats were studied using inclined plane test, Basso-Beattie-Bresnahan (BBB) scale, footprint analysis and video recording images. It was revealed in our research that AAV-5HRE-bFGF-DPSCs has a therapeutic effect on SCI rats via alleviating damage caused by hypoxic microenvironment.

2. Materials and methods

2.1. Reagents and antibodies

Primary mesenchymal stem cell culture system, primary cell culture system and primary rat pericytes were provided by iCell (Shanghai, China). Primary rat astrocytes were provided by OTWO (Shenzhen, China). Dulbecco's modified Eagle's medium (DMEM) and fetal bovine serum (FBS) were bought from Gibco (California, USA). Human-bFGF and *tert*-Butyl hydroperoxide (TBHP) were obtained from Sigma-Aldrich (St. Louis, MO, USA). Primary antibodies to Nestin, Tuj 1, CD13, CD31, PDGFR-β, N-cadherin, HIF-1α, DDC, AMPK-α1, ULK1, LC3-II, P62, NeuN, GAP43, Laminin, Neurocan, GFAP and NF200 were supplied by Abcam (Cambridge, UK). Primary antibodies to bFGF and mTOR were supplied by zenbio (Chengdu, China). Primary antibodies to 5HT-1B, 5HT and STRO-1 were obtained from Affinity Biosciences (OH, USA), Sigma-Aldrich (St. Louis, MO, USA) and Invirogen (California, USA) respectively. Second antibody to anti-rabbit and anti-mouse IgG-conjugated with horseradish peroxidase (HRP), or with Alexa Fluor647 (infrared), Alexa Fluor594 (red), Alexa Fluor488 (green) or Alexa-Fluor405 (blue) were from Abcam (Cambridge, UK). Second antibody anti-mouse IgM-conjugated Alexa Fluor594 (red) and Alexa Fluor488 (green) were from Abcam (Cambridge, UK). Second antibody anti-chicken IgY-conjugated Alexa Fluor488 (green) was from Abcam (Cambridge, UK). An enhanced chemiluminescence (ECL) kit was provided by Bio-Rad (Hercules, CA, USA). DAPI (4′,6-diamidino-2-phenylindole) for cell nuclear staining was from Sigma-Aldrich (St. Louis, MO, USA).

2.2. Isolation of DPSCs and cell culture

Third molars with no periodontal disease, periapical disease or caries were collected from healthy volunteers (20–35 years old, n = 3) at the Department of Oral Surgery, Stomatological Hospital of Wenzhou Medical University with ethical approval (Project No. 2018008). Briefly, 75% alcohol was used to sterilize the tooth surfaces. Dental pulp tissue was collected using dental handpiece, cut into small pieces (approximately 0.5 mm × 0.5 mm × 0.5 mm) then washed three times with PBS containing 2.5% antibiotics. After that, the pulp tissue was digested with 4 mg/ml dispase (Sigma-Aldrich, St. Louis, MO, USA) and 3 mg/ml collagenase type I (Gibco, USA) for 30 min at 37 °C. The cell suspension was collected and maintained in primary mesenchymal stem cell culture system (iCell, Shanghai, China) at a 37 °C incubator with 5% CO_2. The culture medium was replaced five days later, and then the culture medium was changed every two days. Primary pericytes were cultured in primary pericyte culture system (iCell, Shanghai, China) at a 37 °C incubator with 5% CO_2. Primary astrocytes were cultured in DMEM-high glucose containing 10% FBS, 100 U/mL penicillin and 100 μg/ml streptomycin at a 37 °C incubator with 5% CO_2.

2.3. Natural differentiation of DPSCs

DPSCs were plated in a 6-well plate with the density of 1×10^4 cells per well and incubated in a humidified atmosphere containing 5% CO_2 at 37 °C. 24 h later, the cell culture medium was replaced by neuronal induced medium (DMEM-high glucose containing 10% FBS, 100 U/mL penicillin and 100 μg/ml streptomycin) and the cells were maintained for one week. After that, the neuronal induced medium was changed every two days. The cells were evaluated using immunofluorescence staining.

2.4. Cell stimulation

Cells (Naturally differentiated DPSCs, pericytes, astrocytes) were plated in 6-well plates with the density of 5×10^4 cells per well and divided into four groups: (1). Control group, (2). TBHP group, (3). bFGF group and (4). TBHP + bFGF group. The doses of TBHP and bFGF were 20 μM/ml and 50 ng/ml respectively. In TBHP + bFGF group, TBHP and bFGF were administered simultaneously. 24 h after stimulation, the changes of related indexes were analyzed using immunofluorescence and western blotting.

Generation of DPSCs transduced with AAV-mediated and HRE-directed expression of bFGF gene.

AAV-5HRE-bFGF or AAV-5HRE vectors were prepared using pAOV001 PAAV-CAG-MCS stem plasmid at clone sites of Mlu I and Hind III by Obio outsourcing service (Shanghai, China). The AAV-5HRE-bFGF or AAV-5HRE vectors were confirmed by DNA sequencing. 5HRE, representing five repeats of HRE DNA sequence, was located at upstream of the minimum promoter of cytomegalovirus (CMV). The AAV virus particles were produced by Obio's outsourcing service (Shanghai,

China). In brief, AAV-5HRE-bFGF or AAV-5HRE plasmids and the helper plasmid pAAV-RC were co-transfected into HEK293 cells. The virus particles were purified using caesium chloride density gradient followed by dialysis. Then Quantitative polymerase chain reaction (qPCR) was performed to have the virus titers tested. It was suggested that stocks of AAV-5HRE-bFGF and AAV-5HRE contain virus particles with a titer of 2.62×10^{12} and 2.35×10^{12}/ml respectively. After that, DPSCs were transduced with 1×10^5 multiplicity of infection (MOI) of AAV-5HRE-bFGF and AAV-5HRE virus particles respectively, which were repeatedly estimated to achieve a 90% transduction rate. Transduced cells were cultured in normoxic or hypoxic (<1% O_2) condition for hypoxia induced expression for at least 6 h. The protein concentration of cultured supernatant was measured using bFGF enzyme-linked immunosorbent assay (ELISA) kit (Institute of Immunology, Tokyo, Japan).

2.5. Rat model of SCI

Sprague-Dawley rats were anesthetized with 5% isoflurane until unconscious followed by 3% isoflurane during surgery. The T9-T10 spinous and laminoid processes were removed to have the spinal cord exposed. Centered on the posterior median line, a 10g hammer was used to impinge the T9 segment of the spinal cord from a height of 25 mm to induce acute SCI. Rats in sham group received only laminectomy but not heavy blow procedure. The rats were intraperitoneally injected with cefazolin sodium (0.9%) twice daily and assisted to urinate artificially in every morning and evening.

2.6. DPSCs transplantation

Sprague-Dawley rats were randomly divided into four groups: (1). Sham group, (2). SCI group, (3), AAV-5HRE-DPSCs group (CON-DPSCs) and (4). AAV-5HRE-bFGF-DPSCs group (bFGF-DPSCs). Each group contained 18 rats. DPSCs were pre-transduced with 1×10^5 MOI of AAV-5HRE-bFGF or AAV-5HRE virus particles for 48 h. Seven days after SCI, the spinal cord was re-exposed, and 5×10^5 DPSCs re-suspended in 10 μl cold PBS were injected into the SCI center (depth: 1 mm) by stereotaxic instrument and micro injection pump. Functional recovery of SCI was evaluated at day 1, day 3, day 7, day 10, day 14, day 21 and day 30 after DPSCs transplantation. Six random rats at each time point were used for evaluating functional recovery of SCI. Rats were sacrificed both 14 and 30 days after DPSCs transplantation for Western blot, histology and immunofluorescence staining.

2.7. Evaluation of functional recovery of SCI rats

The recovery of spinal cord function in rats was evaluated by BBB score, oblique plate test, footprint and video recording images. The rats were placed on a platform and allowed to move freely. The hind limb walking and limb movement were recorded to have the BBB scores evaluated. To perform the inclined plate test, an inclined plate which can adjust activity was preset on the desktop. The rats were placed on a 6 mm thick anti-skid pad, and the vertical axis of rat body and the long axis of inclined plate were perpendicular to each other. The angle between the desktop and the inclined plate was slowly raised until the rats could be on board for 5 s, and then the angle was recorded it. A 7.5 cm × 100 cm track was set up and covered with white paper. The track was covered with black plastic film to avoid light, so as to meet the adaptability of rats to the dark environment. The rats whose hind feet were marked with red dye were placed at the starting point of the track and allowed to move from one end to the other. The footprints were observed to have motor function evaluated. Video images were recorded and quantitatively analyzed as previously described [12], including weight support, leg extensor spasms, the number of footsteps and the posture of the foot.

2.8. Nissl and H&E staining

Thoracotomy was performed on a randomly selected portion of SCI rats 30 days after the cell transplantation (d.a.t.). The heart was infused with 500 ml paraformaldehyde buffer solution, then the spinal cord was carefully separated. The spinal cord was fixed in 4% paraformaldehyde for two days. The tissue was then sectioned (5 μm) and stained for histopathological examination using Hematoxylin and eosin (H&E) and Nissl staining. For Nissl staining, the sections were stained with tar purple dye for 30 min then incubated at 37 °C for 15 min. After being rinsed with distilled water and 95% alcohol, the sections were treated with conventional dehydration, transparency and tablet sealing. Images were observed and photographed using an optical microscope.

2.9. Western blot analysis

Tissue was isolated from the central regions of the spinal cord injury and rapidly stored at −80 °C for Western blot assays. The tissues were homogenized in modified radioimmunoprecipitation assay (RIPA) buffer (50 mM Tris-HCl, 1% Nonidet P-40, 20 mM DTT, 150 mM NaCl, pH = 7.4) which contains 10 μl/ml protease inhibitor cocktail (GE Healthcare Biosciences, PA, USA). The extracts were then centrifuged at 12,000 rpm and the supernatant was collected for protein assay. Similarly, *in vitro* cultured DPSCs, pericytes, astrocytes were lysed in RIPA buffer (25 mM Tris-HCl, 150 mM NaCl, 1% Nonidet P-40, 1% sodium deoxycholate, and 0.1% SDS) to have proteins extracted. The protein concentration was quantified with bicinchoninic acid (BCA) reagents (Thermo, Rockford, IL, USA). 40 μg protein per lane was used to load on a 10% gel and then transferred onto a polyvinylidene fluoride (PVDF) membrane (Bio-Rad, Hercules, CA, USA). The membrane, pre-incubated with 5% milk (Bio-Rad) in Tris-buffered saline (TBS) with 0.05% Tween 20 for 2 h, was incubated with each of following antibodies: anti-N-cadherin (1:1000), anti-AMPK-α1 (1:1000), anti-ULK1 (1:1000) anti-mTOR (1:1000), anti-LC3 (1:1000) and GAPDH (1:5000) at 4 °C overnight. After that, the membranes were washed with TBST three times then incubated with HRP-conjugated secondary antibodies at room temperature for 2 h. Signals were detected by ChemiDoc XRS + Imaging System (Bio-Rad) and band densities were measured using Multi Gauge Software of Science Lab 2006 (FUJIFILM Corporation, Tokyo, Japan) and quantified by Quantity One (version 4.5.2; Bio-Rad).

2.10. Immunofluorescence staining

The harvested spinal cord was fixed in 4% paraformaldehyde for two days, followed by paraffin embedding and sectioning. The sections were dried then washed twice with xylene to have paraffin removed. After hydrated with gradient alcohols, samples were rinsed with PBS for three times and then incubated with H_2O_2 for 30 min. Then, the tissue was permeabilized with PBS plus 0.5% Triton X 100 (PBST), sealed with 1% bovine serum albumin (BSA) and incubated with primary antibodies at 4 °C overnight. Negative controls were incubated with incubation solution without primary antibody. In the next day, the samples were washed with PBST and incubated with corresponding secondary antibody conjugated with Alexa Fluor647 (infrared), Alexa Fluor594 (red), Alexa Fluor488 (green) or Alexa-Fluor405 (blue) at 37 °C for 1 h. DAPI was employed to stain the cell nuclei. After the reaction was quenched, the sections were sealed and stored at 4 °C. Photographs were taken using a fluorescence microscope. Fluorescent images were taken from the regions of interests (ROI) in comparable matching anatomical regions between groups. ROI from six samples in each group was analyzed using Imagine J software and the statistical graphs were generated using Prism 7 (GraphPad, San Diego, CA).

2.11. Statistical analysis

Generalized linear mixed models were used to analyze BBB scores

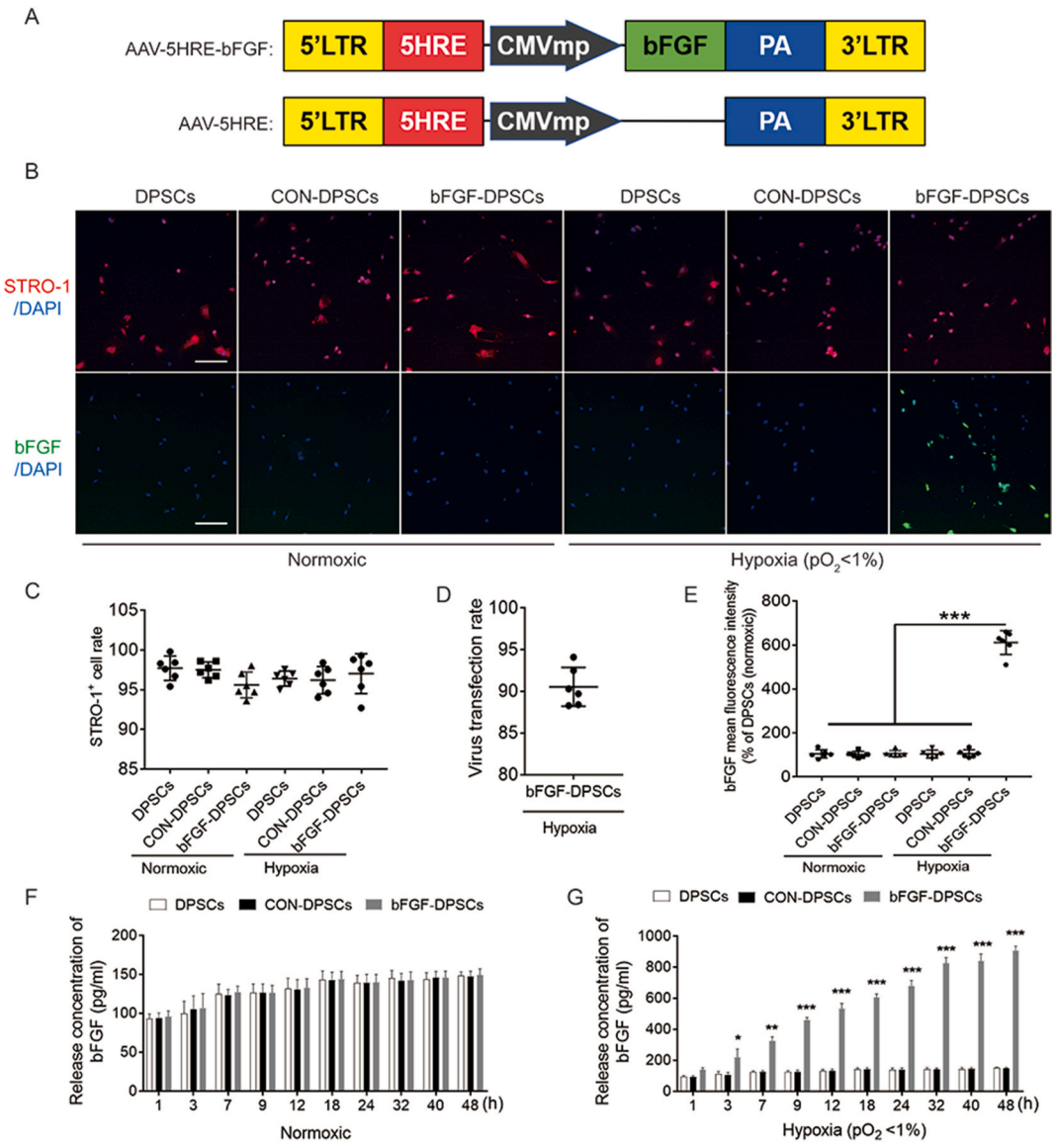

Fig. 1. Preparation, characterization and differential detection of AAV-5HRE-bFGF-DPSCs. (A) Schematic diagrams showing the vector construction: AAV-5HRE-bFGF and AAV-5HRE. **(B)** Immunofluorescence staining showing STRO-1 (red) and bFGF (green) in the DPSCs group, CTRL group and bFGF group under normoxic and hypoxic conditions. The nucleus is labeled by DAPI (blue). Magnification:10X; Scale bar: 200 μm. **(C)** Quantitative analyses of immunofluorescence staining showing the fluorescence intensity of STRO-1 positive cells under normoxic and hypoxic conditions. **(D)** The virus transfection rate of bFGF. **(E)** Comparison of tThe fluorescence intensity of bFGF positive cells in different groups under normoxic and hypoxic conditions. **(F–G)** ELISA results showing bFGF release concentration of DPSCs group, CTRL group and bFGF group under normoxic and hypoxic conditions. The nucleus is labeled by DAPI (blue). Magnification:10X; Scale bar: 200 μm * represents $P < 0.05$. ** represents $P < 0.01$. *** represents $P < 0.001$. Data are represented as mean ± SD ($n = 6$). (For interpretation of the references to colour in this figure legend, the reader is referred to the Web version of this article.)

and inclined plane test. Two-sided Student's *t*-test was performed when the experiment has two groups for data comparisons. Analysis of variance and Turkey' *post hoc* analyses were used when the experiment has more than two groups for data comparisons. Software including Excel and GraphPad Prism 7 were used for statistical analyses. Data were represented as mean ± Standard deviation (SD). $P < 0.05$ represents statistical difference.

3. Results

3.1. AAV-mediated and HRE-directed expression of bFGF gene in DPSCs

To investigate if AAV-mediated bFGF expression is in a hypoxia-inducible manner under the direct regulation of HRE, an AAV-5HRE-bFGF construct was generated and transduced it into DPSCs (Fig. 1A). Differentiation state of DPSCs were investigated with STRO-1 used to mark DPSCs. CD13, CD31, Nestin, glial fibrillary acidic protein (GFAP), NeuN and beta 3 tubulin (Tuj 1) were used to detect the nerve and vascular indexes. DPSCs were shown not differentiate into other neurogenic or vascular-derived cells after transduction (Fig. S1). Indicated by staining results, STRO-1 expression ratio is not statistically different among the DPSCs group, AAV-5HRE-DPSCs (CON-DPSCs) group and AAV-5HRE-bFGF-DPSCs (bFGF-DPSCs) group under normoxic and hypoxic condition (Fig. 1B and C). The transduction rate of AAV-5HRE-bFGF reached 90.55 ± 2.32% and bFGF protein expression in bFGF-DPSCs group was induced by hypoxia *in vitro* but not by normoxia when compared with CON-DPSCs group (Fig. 1B, D, E). Furthermore, time course experiments were conducted to have the bFGF protein expression level investigated, which revealed that the bFGF expression of bFGF-DPSCs group was induced by hypoxia but not by

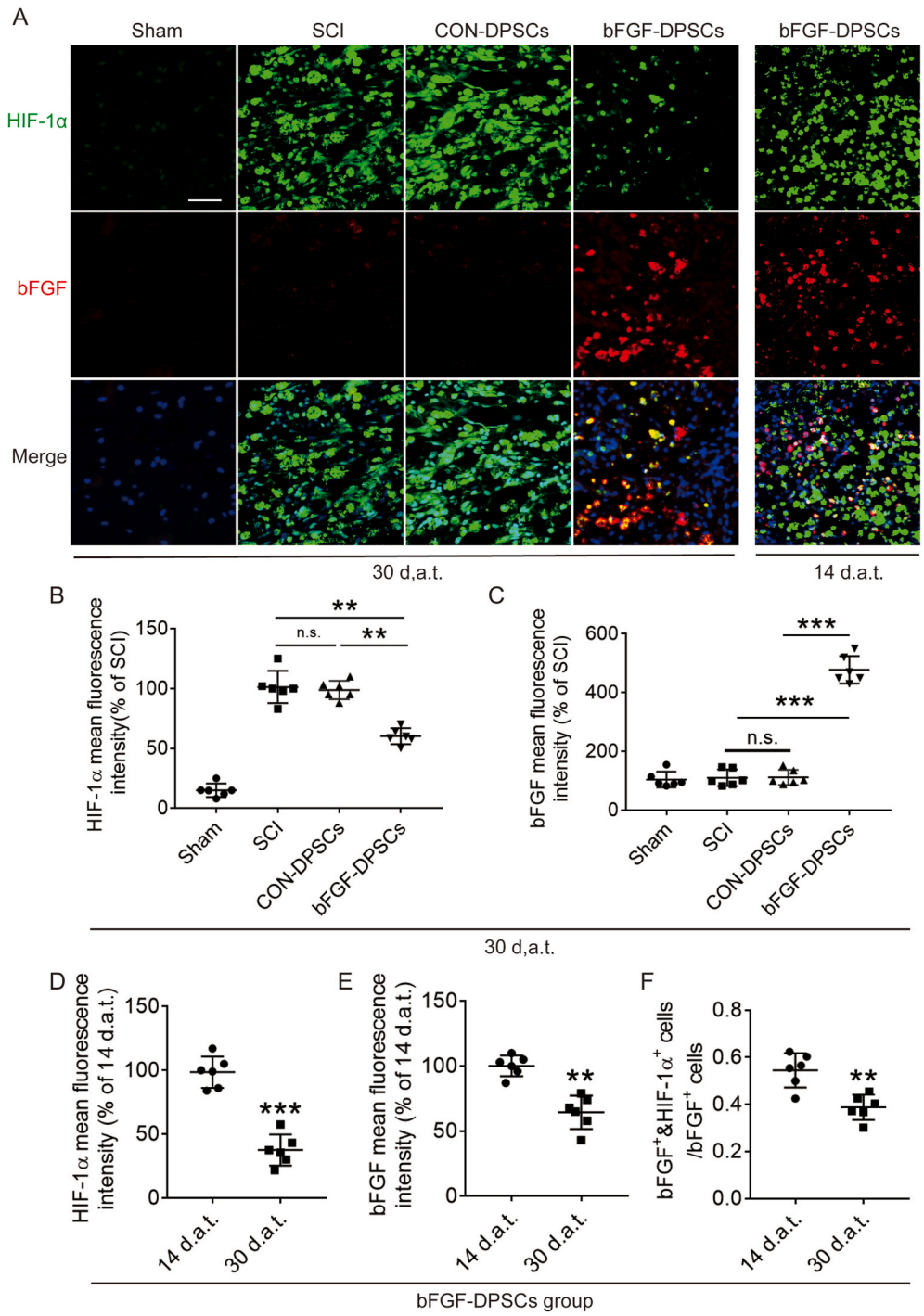

Fig. 2. Functional verification of AAV-5HRE-bFGF-DPSCs *in vivo*. **(A)** Immunofluorescence staining showing HIF-1α (green) and bFGF (red) in the Sham, SCI group, AAV-5HRE-DPSCs (CON-DPSCs) group and AAV-5HRE-bFGF-DPSCs (bFGF-DPSCs) group in 30 d.a.t. and bFGF-DPSCs group in 14 d.a.t.. The nucleus is labeled by DAPI (blue). Magnification: 40X; Scale: 50 μm. **(B–C)** The fluorescence intensity of HIF-1α and bFGF in the Sham, SCI group, CON-DPSCs group and bFGF-DPSCs group in 30 d.a.t.. **(D–E)** The fluorescence intensity of HIF-1α and bFGF in 14 and 30 d.a.t.. **(F)** The ratio of HIF-1α$^+$ & bFGF$^+$ cells in bFGF$^+$ cells in 14 and 30 d.a.t.. * represents $P < 0.05$. ** represents $P < 0.01$. *** represents $P < 0.001$. n.s. represents no statistical significance. Data are represented as mean ± SD (n = 6). (For interpretation of the references to colour in this figure legend, the reader is referred to the Web version of this article.)

normoxia in a time course dependent manner when compared with DPSCs or CON-DPSCs group (Fig. 1F and G). Collectively, it was indicated by all these results that AAV-5HRE-bFGF was successfully transfected into DPSCs, with bFGF expressed only under the hypoxic condition.

3.2. The bFGF expression of bFGF-DPSCs group is regulated by hypoxia in vivo

In order to investigate the bFGF and HIF-1α expression after bFGF-DPSCs transplantation in SCI rats, bFGF and HIF-1α was immunostained. It was revealed that HIF-1α positive rate in the SCI group was the highest among all the groups at 14 d.a.t. and 30 d.a.t.. The HIF-1α positive rate of the CON-DPSCs group was similar to the SCI group with no statistical significance revealed. The HIF-1α positive rate of the bFGF-DPSCs group was significantly lower than that of the SCI group at both day 14 and day 30 (Fig. 2A and B). At the same time, the bFGF positive rate of bFGF-DPSCs group was significantly higher when compared with the SCI group and CON-DPSCs group (Fig. 2A, C). To further explore the origin of decreased HIF-1α positive rate in the bFGF-DPSCs group, we comprehensively analyzed HIF-1α and bFGF expression. It was revealed that the HIF-1 α positive rate (Fig. 2A, D) and the bFGF positive rate (Fig. 2A, E) showed a similar trend, decreasing over time in the bFGF-DPSCs group. In addition, the proportion of bFGF$^+$ & HIF-1α$^+$ cells in bFGF$^+$ cells were shown to decrease over time (Fig. 2A, F). To sum up, AAV-5HRE-bFGF-DPSCs express high level of bFGF *in vivo* and the bFGF

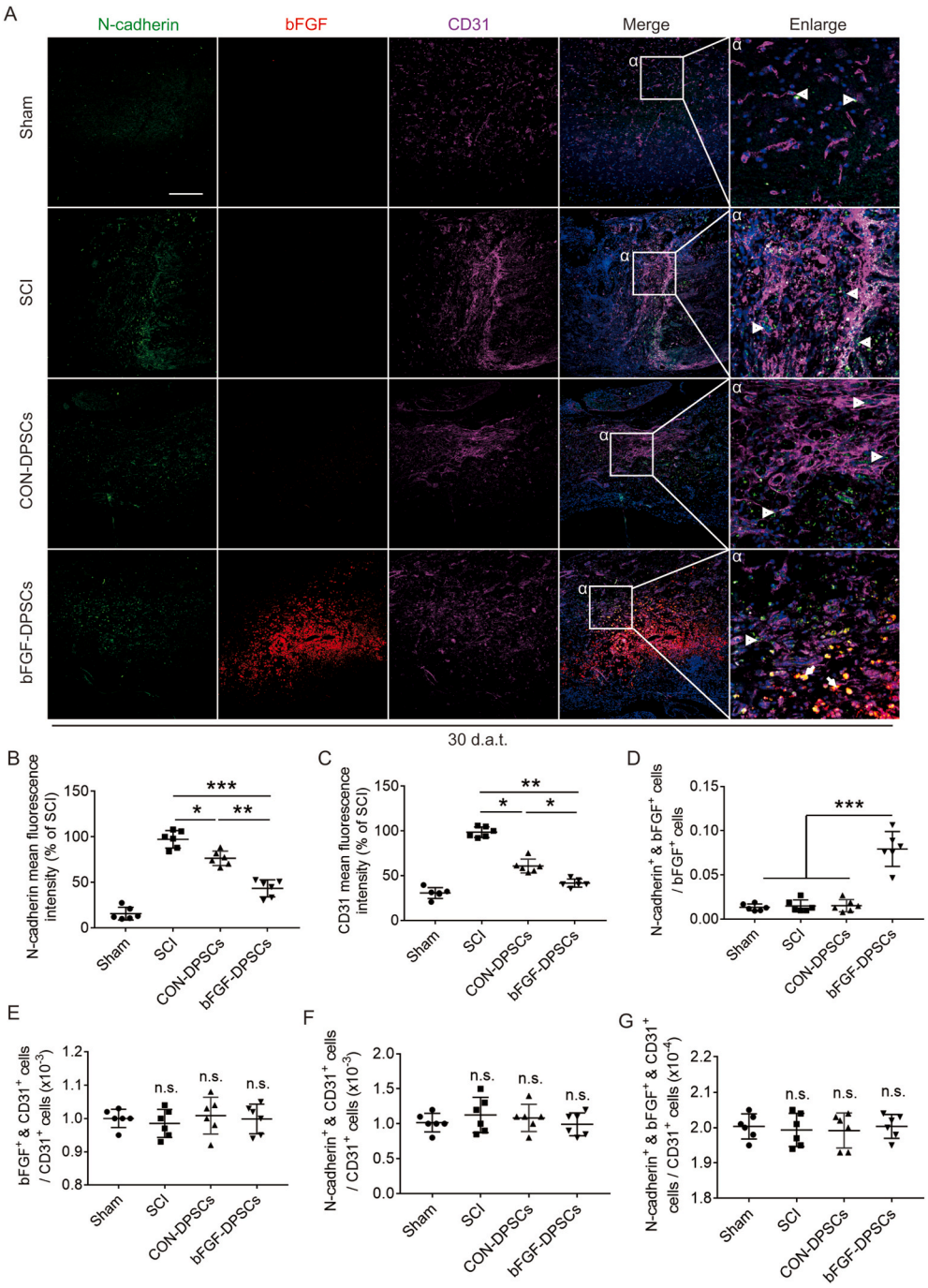

Fig. 3. Analysis of the relationship between AAV-5HRE-bFGF-DPSCs and vascular endothelial cells. **(A)** Immunofluorescence staining showing the expression of N-cadherin (green), bFGF (red) and CD31 (purple) in the Sham, SCI group, AAV-5HRE-DPSCs (CON-DPSCs) group and AAV-5HRE-bFGF-DPSCs (bFGF-DPSCs) group at day 30. The nucleus is labeled by DAPI (blue). Magnification: 20X; Scale: 100 μm. **(B–C)** Comparison of the fluorescence intensity of N-cadherin and CD31 of positive cells (relative to SCI group). **(D–G)** The ratio of different cells in the Sham, SCI group, AAV-5HRE-DPSCs (CON-DPSCs) group and AAV-5HRE-bFGF-DPSCs (bFGF-DPSCs) group. * represents $P < 0.05$. ** represents $P < 0.01$. *** represents $P < 0.001$. n.s. represents no statistical significance. Data are represented as mean ± SD ($n = 6$). (For interpretation of the references to colour in this figure legend, the reader is referred to the Web version of this article.)

expression in bFGF-DPSCs group was accompanied by the decreased HIF-1α expression, indicating that the expression of bFGF was regulated by hypoxia environment and bFGF might be involved in promoting the recovery of hypoxic environment in SCI rats.

3.3. Endothelial cells are not involved in the recovery of hypoxia environment in SCI

The expression of N-cadherin and CD31 was investigated using immunofluorescence staining 30 d.a.t., with bFGF used to mark AAV-5HRE-bFGF-DPSCs. It was revealed that CD31 and N-cadherin positive rate of the SCI group were the highest among all four groups. Meanwhile, the CD31 and N-cadherin positive rate of the bFGF-DPSCs group were significantly lower than that of the SCI group and CON-DPSCs group (Fig. 3A–C). The cells expressing N-cadherin did not co-express CD31, but partially co-expressed bFGF (N-cadherin$^+$ & bFGF$^+$ cells) (Fig. 3A). To explore hypoxia recovery related factors, further analysis was conducted. It was indicated that the N-cadherin expression rate in bFGF$^+$ cells of the bFGF-DPSCs group was significantly higher when compared with other groups and N-cadherin$^+$ & bFGF$^+$ cells were located around the vessels (Fig. 3A, D). In the analysis of endothelial cells, it was found that the positive rate of bFGF and N-cadherin in endothelial cells of each group was not statistically different (Fig. 3A, E-G). Suggested by all the analyses, N-cadherin$^+$ perivascular cells that are differentiated from the transplanted DPSCs may be the key to hypoxia relief.

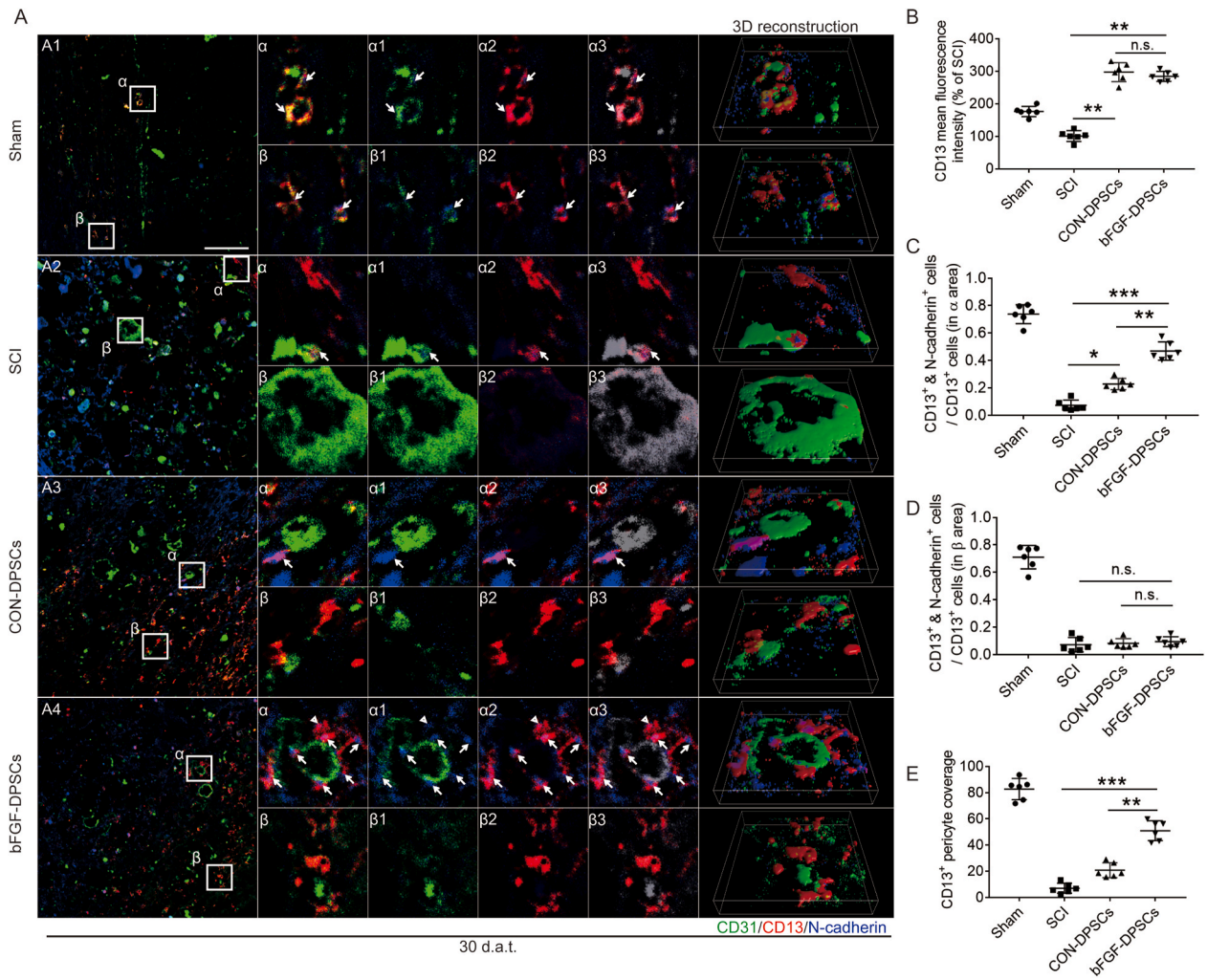

Fig. 4. CD13$^+$ pericytes rely on N-cadherin to attach to vascular endothelial cells. **(A)** Immunofluorescence staining showing the expression of CD31 (green), CD13 (red) and N-cadherin (blue) in the Sham, SCI group, AAV-5HRE-DPSCs (CON-DPSCs) group and AAV-5HRE-bFGF-DPSCs (bFGF-DPSCs) group. α1 and β1 represent the fitting of CD31 and N-cadherin. α2 and β2 represent the fitting of CD13 and N-cadherin. α3 and β3 represent the fitting of CD31, CD13 and N-cadherin (green becomes gray). Magnification: 40X; Scale: 50 μm. **(B)** The fluorescence intensity of CD13 in different groups. **(C–D)** The ratio of N-cadherin$^+$ & CD13$^+$ pericytes in CD13$^+$ pericytes in α and β areas. **(E)** The coverage of CD13$^+$ pericyte. * represents $P < 0.05$. ** represents $P < 0.01$. *** represents $P < 0.001$. n.s. represents no statistical significance. Data are represented as mean ± SD (n = 6). (For interpretation of the references to colour in this figure legend, the reader is referred to the Web version of this article.)

3.4. CD13$^+$ pericytes are the key targets for regulating hypoxic microenvironment after SCI

Previous studies have shown that PDGFR-β$^+$ pericytes are related to vascular penetration [34,35], which might be related to regulation of hypoxic environment after SCI. Here, the distribution of PDGFR-β$^+$ pericytes in the sham group and the SCI group were investigated 3, 14 and 30 d.p.i., with the result showing that the number of endothelial cells and PDGFR-β$^+$ increased over time (Fig. S2A,B). However, the coverage of PDGFR-β$^+$ pericytes 3, 14 and 30 d.p.i. was not statistically different when compared with the sham group (Fig. S2A,C). Hence, PDGFR-β$^+$ pericytes are not significantly related to the recovery of hypoxia environment after SCI.

On another hand, it has been reported previously that CD13$^+$ pericytes could regulate the blood flow speed of micrangium via contraction [12]. To investigate if CD13$^+$ pericytes are involved in regulating hypoxic environment after SCI, the expression of N-cadherin and CD13 was analyzed using immunofluorescence staining at day 30. Endothelial cells were stained using CD31. It was revealed that the expression of CD13 in two DPSCs transplantation groups was not statistically different but was significantly higher than the sham group and the SCI group (Fig. 4A and B). According to immunofluorescence staining, cells expressing N-cadherin were partially colocalized with CD13$^+$ pericytes but not with CD31$^+$ endothelial cells, suggesting that N-cadherin was secreted by CD13$^+$ pericytes (Fig. 4A: α1, β1; α2, β2; α3, β3 and 3D reconstruction).

The expression of CD13$^+$ pericytes varied in spatial distribution, which can be divided into surrounding endothelial cells (α area) and scattered distribution (β area). To further explore the N-cadherin expression of CD13$^+$ pericytes in different areas, the N-cadherin expression of CD13$^+$ pericytes in α and β area was analyzed. It was revealed in α area that the proportion of CD13$^+$ pericytes secreting N-cadherin was highest in the sham group, followed by which was the bFGF-DPSCs group, and the SCI group was the lowest (Fig. 4A, C). In contrast, the proportion of CD13$^+$ pericytes expressing N-cadherin was equally low in the SCI group, CON-DPSCs group and bFGF-DPSCs group (Fig. 4A, D). In addition, the coverage of CD13$^+$ pericytes in the sham group was the highest, followed by the bFGF group (Fig. 4A, E), which was consistent with the expression pattern of CD13$^+$&N-cadherin$^+$ cells in α area. It was indicated by these data that N-cadherin might play an important role in helping CD13 adhere to endothelial cells.

To further investigate if CD13$^+$ pericytes are involved in regulating the hypoxia microenvironment in SCI, HIF-1α and CD13 were

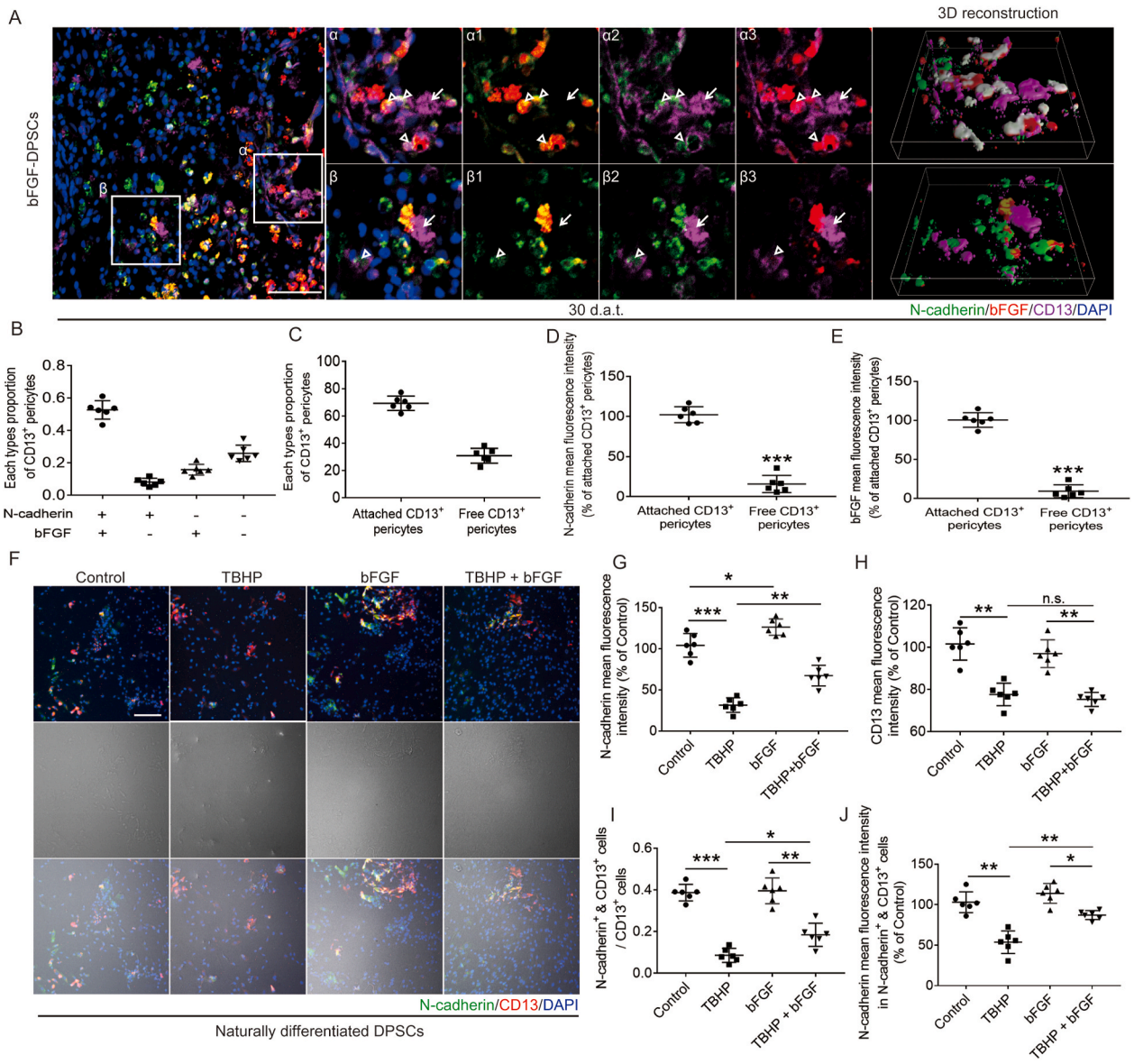

Fig. 5. AAV-5HRE-bFGF-DPSCs up-regulate N-cadherin in CD13$^+$ pericytes via secreting bFGF. **(A)** Immunofluorescence staining showing the expression of N-cadherin (green), bFGF (red), CD13 (purple) and DAPI (blue) in the Sham, SCI group, AAV-5HRE-DPSCs (CON-DPSCs) group and AAV-5HRE-bFGF-DPSCs (bFGF-DPSCs) group. α1 and β1 represent the fitting of N-cadherin and bFGF. α2 and β2 represent the fitting of N-cadherin and CD13. α3 and β3 represent the fitting of bFGF and CD13. Magnification: 40X; Scale: 50 μm. **(B–C)** Analysis of different types of CD13 positive cells. **(D–E)** The fluorescence intensity of N-cadherin and bFGF in CD13 positive pericytes. **(F)** Immunofluorescence staining showing the expression of N-cadherin (green), CD13 (red) and DAPI (blue) in the Control group, TBHP group, bFGF group and TBHP + bFGF group (The cells are naturally differentiated DPSCs). Magnification: 40X; Scale: 50 μm. **(G–H)** The fluorescence intensity of N-cadherin and CD13. **(I)** The ratio of N-cadherin$^+$ & CD13$^+$ pericytes in CD13$^+$ pericytes. **(J)** The fluorescence intensity of N-cadherin in N-cadherin$^+$ & CD13$^+$ pericytes. * represents $P < 0.05$. ** represents $P < 0.01$. *** represents $P < 0.001$. n.s. represents no statistical significance. Data are represented as mean ± SD (n = 6). (For interpretation of the references to colour in this figure legend, the reader is referred to the Web version of this article.)

immunostained. Interestingly, CD13 expression level was the highest in both CON-DPSCs group and bFGF-DPSCs group while HIF-1α expression level in bFGF-DPSCs group was significantly lower than that in CON-DPSCs group (Fig. S3A,B,C). In bFGF-DPSCs group, CD13$^+$ pericytes surrounded to form a tube (tubular pericytes) with no significant statistical difference revealed when compared with the Sham group, and little HIF-1α was expressed in the center of the tube (Fig. S3A: α asterisk marker, E). In the CON-DPSCs group, the CD13$^+$ pericytes morphology remained round (S Fig. 2A: α). In contrast, the CD13$^+$ pericytes morphology was long and flat in the Sham group. In order to further explore the reason why the number of CD13$^+$ pericytes in the bFGF-DPSCs group was higher than that in the SCI group, AAV-5HRE-bFGF-DPSCs were labeled with bFGF. It was revealed by immunofluorescence staining that bFGF is co-localized with the tubular pericytes as described above (Fig. S3A: α, α1). Furthermore, the immunofluorescence staining of CD13, HIF-1α and bFGF in bFGF-DPSCs group was performed 14 d.a.t., showing that the expression pattern of CD13$^+$ pericytes was changed from scattered distribution (free pericytes) to tubular existence (tubular pericytes) 14 d.a.t.. Moreover, bFGF was co-localized with the tubular pericytes and the bFGF expression in free pericytes 14 d.a.t., which was significantly lower than tubular pericytes 14 and 30 d.a.t. (Fig. S3D: α, α1; F). After being transplanted into the injured spinal cord, DPSCs differentiated into CD13$^+$ pericytes. We hypothesized that bFGF expressed by AAV-5HRE-bFGF-DPSCs can promote the recovery of hypoxia microenvironment in SCI via upregulating N-cadherin to promote CD13 adhesion to vascular endothelial

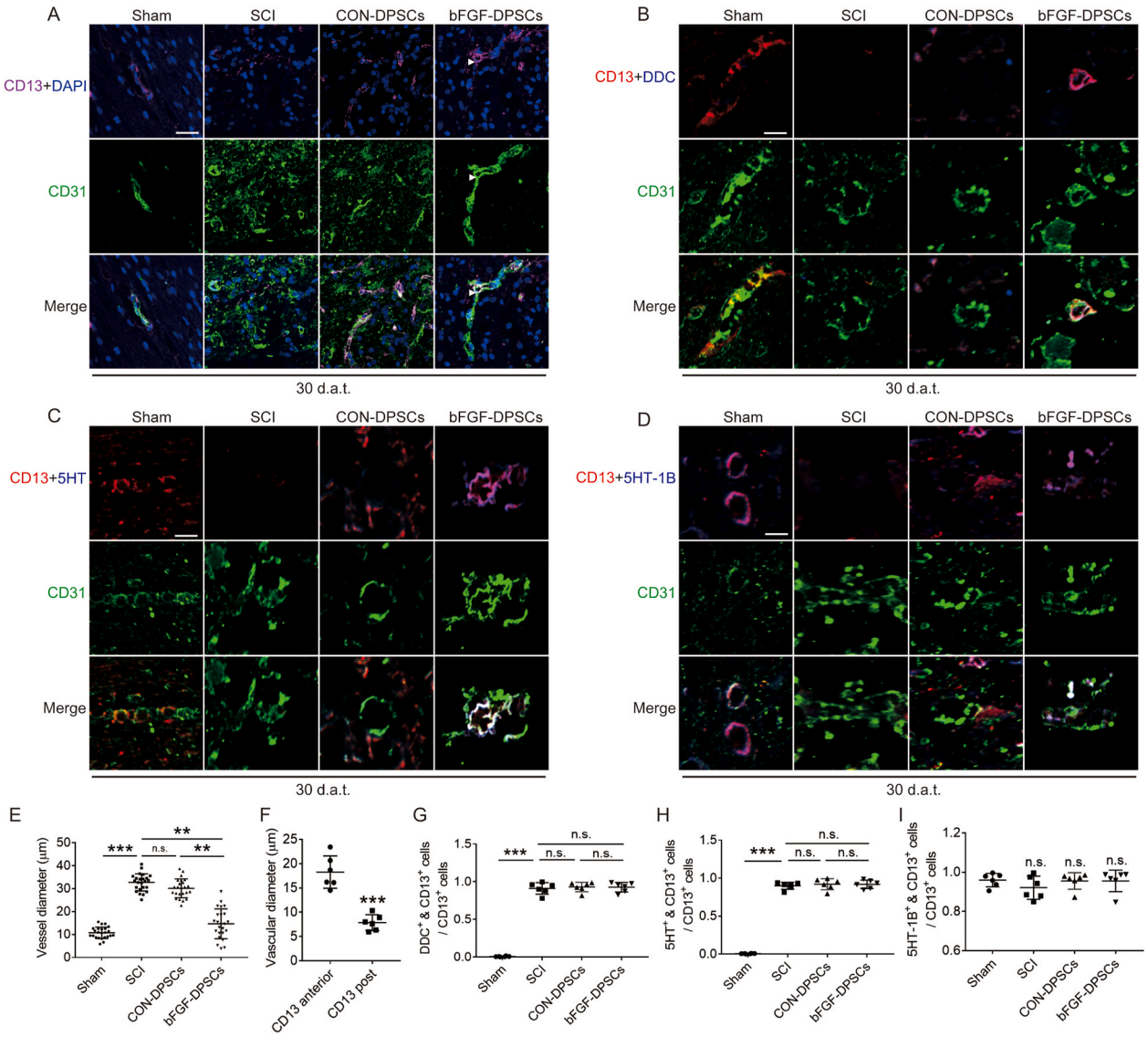

Fig. 6. CD13 constricts blood vessels through the DDC-5HT-5HT-1B pathway. **(A)** Immunofluorescence showing the expression of CD13 (purple), CD31 (green) and DAPI (blue) in the Sham, SCI group, AAV-5HRE-DPSCs (CON-DPSCs) group and AAV-5HRE-bFGF-DPSCs (bFGF-DPSCs) group. Magnification: 40X; Scale: 50 μm. **(B)** Immunofluorescence staining showing the expression of CD13 (red), DDC (purple), CD31 (green) and DAPI (blue) in the Sham, SCI group, AAV-5HRE-DPSCs (CON-DPSCs) group and AAV-5HRE-bFGF-DPSCs (bFGF-DPSCs) group. Magnification: 160X; Scale: 12.5 μm. **(C)** Immunofluorescence staining showing the expression of CD13 (red), 5HT (purple), CD31 (green) and DAPI (blue) in the Sham, SCI group, CON-DPSCs group and bFGF-DPSCs group. Magnification: 160X; Scale: 12.5 μm. **(D)** Immunofluorescence staining showing the expression of CD13 (red), 5HT-1B (purple), CD31 (green) and DAPI (blue) in the Sham, SCI group, CON-DPSCs group and bFGF-DPSCs group. Magnification: 160X; Scale: 12.5 μm. **(E)** The blood vessel diameter in the Sham, SCI group, CON-DPSCs group and bFGF-DPSCs group. * represents $P < 0.05$. ** represents $P < 0.01$. *** represents $P < 0.001$. Data are represented as mean ± SD (n = 24). **(F)** The vessel diameter of CD13 anterior vessel and CD13 post vessel. **(G–I)** The ratio of different type of CD13 positive cells in CD13 positive cells. * represents $P < 0.05$. ** represents $P < 0.01$. *** represents $P < 0.001$. n.s. means no statistical significance. Data are represented as mean ± SD (n = 6). (For interpretation of the references to colour in this figure legend, the reader is referred to the Web version of this article.)

cells.

bFGF promotes the secretion of N-cadherin from $CD13^+$ pericytes *in vivo* and *in vitro*.

In order to explore the mechanism of N-cadherin secretion by $CD13^+$ pericytes, we focused on the relationship between N-cadherin and bFGF in the bFGF-DPSCs group. The expression of N-cadherin, bFGF and CD13 30 d.a.t. was analyzed using immunofluorescence staining and the cells were divided into four types: N-cadherin$^+$ & bFGF$^+$ & CD13$^+$ pericytes, N-cadherin$^+$ & bFGF$^-$ & CD13$^+$ pericytes, N-cadherin$^-$ & bFGF$^+$ & CD13$^+$ pericytes and N-cadherin$^-$ & bFGF$^-$ & CD13$^+$ pericytes. According to spatial distribution, $CD13^+$ pericytes were also classified into attached pericytes and free pericytes. It was shown that most of the N-cadherin$^+$ & bFGF$^+$ & CD13$^+$ pericytes and N-cadherin$^+$ & bFGF$^-$ & CD13$^+$ pericytes are attached pericytes while most of the N-cadherin$^-$ & bFGF$^+$ & CD13$^+$ pericytes and N-cadherin$^-$ & bFGF$^-$ & CD13$^+$ pericytes are free pericytes. In addition, the co-expression of bFGF and N-cadherin was revealed to be more common in the attached $CD13^+$ pericytes (Fig. 5A: α1, α2, α3 and 3D reconstruction) and the expression level of bFGF and N-cadherin was significantly lower in free pericytes (Fig. 5A: β1, β2, β3 and 3D reconstruction; D, E). Thus, we concluded that DPSCs differentiate into $CD13^+$ pericytes and secrete bFGF to improve the expression of N-cadherin, promoting the adhesion of $CD13^+$ pericytes to vascular endothelial cells.

Furthermore, cell experiments were conducted to investigate the effects of bFGF on N-cadherin in $CD13^+$ pericytes. Six days after being naturally induced, DPSCs were shown to differentiate into $CD13^+$

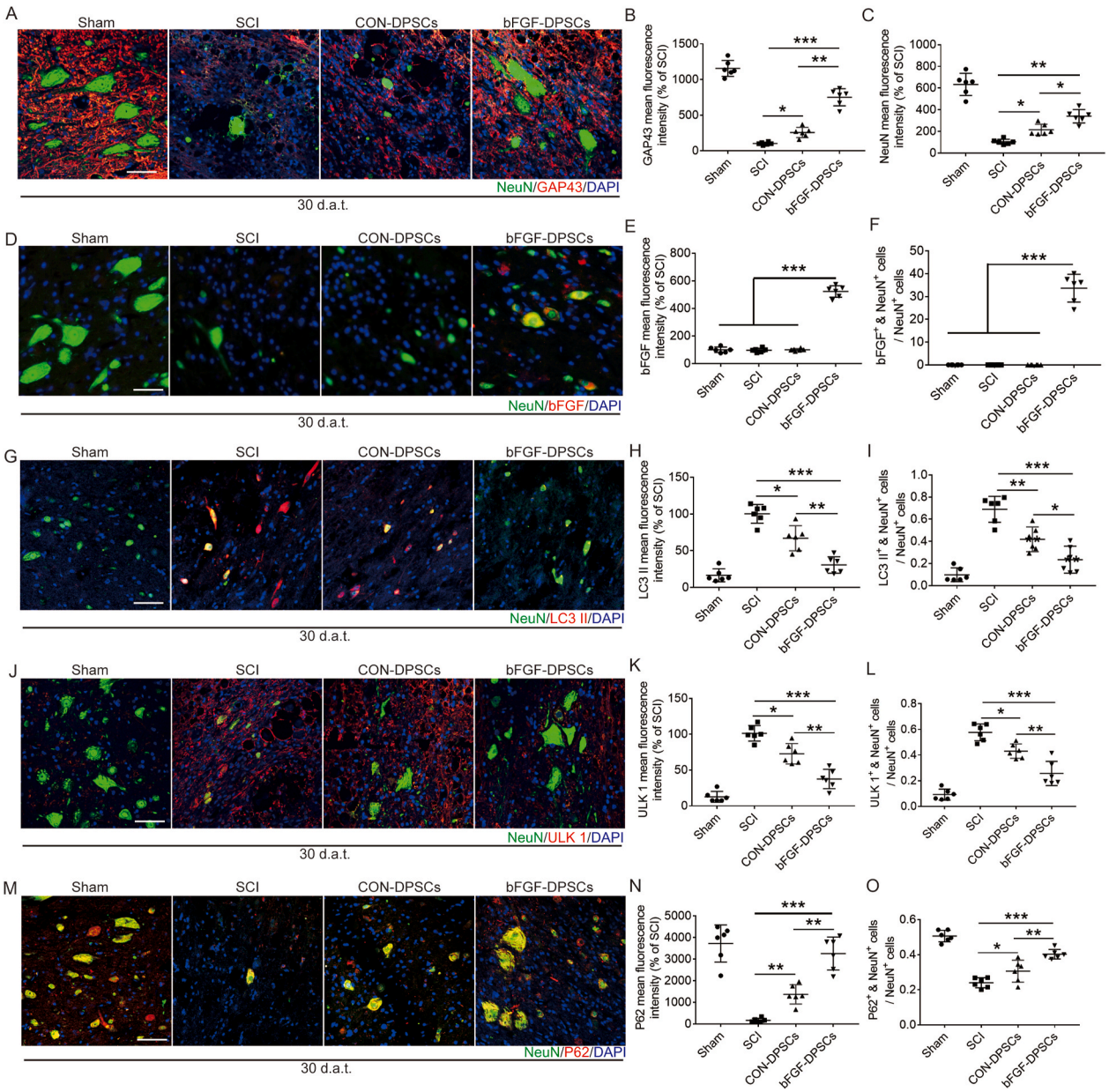

Fig. 7. AAV-5HRE-bFGF-DPSCs up-regulate the expression of NeuN and GAP43, differentiate into neurons and inhibite autophagy. **(A)** Immunofluorescence staining showing the expression of NeuN (green), GAP43 (red) and DAPI (blue). Magnification: 40X; Scale bar: 50 μm. **(B–C)** The fluorescence intensity of NeuN and GAP43 in different groups. **(D)** Immunofluorescence staining showing the expression of NeuN (green), bFGF (red) and DAPI (blue). Magnification: 40X; Scale bar: 50 μm. **(E)** The fluorescence intensity of bFGF in different groups. **(F)** The ratio of bFGF$^+$ & NeuN$^+$ cells in NeuN$^+$. **(G)** Immunofluorescence staining showing the expression of NeuN (green), LC3 II (red) and DAPI (blue). Magnification: 40X; Scale: 50 μm. **(H)** The fluorescence intensity of LC3 II in different groups. **(I)** The ratio of LC3 II$^+$ & NeuN$^+$ cells in NeuN$^+$ cells. **(J)** Immunofluorescence staining showing the expression of NeuN (green), ULK1 (red) and DAPI (blue). Magnification: 40X; Scale: 50 μm. **(K)** The fluorescence intensity of ULK1 in different groups. **(L)** The ratio of ULK1$^+$ & NeuN$^+$ cells in NeuN$^+$ cells. **(M)** Immunofluorescence staining showing the expression of NeuN (green), P62 (red) and DAPI (blue). Magnification: 40X; Scale: 50 μm. **(N)** The fluorescence intensity of P62 in different groups. **(O)** The ratio of P62$^+$ & NeuN$^+$ cells in NeuN$^+$ cells. * represents $P < 0.05$. ** represents $P < 0.01$. *** represents $P < 0.001$. n.s. means no statistical significance. Data are represented as mean ± SD (n = 6). (For interpretation of the references to colour in this figure legend, the reader is referred to the Web version of this article.)

pericytes *in vitro*. Then, DPSCs were treated with different drugs and the expression of CD13$^+$ and N-cadherin was investigated. After treated with TBHP, both the expression of CD13$^+$ and N-cadherin decreased when compared with the control group (Fig. 5A, G, H). In the bFGF group, the expression of N-cadherin increased but the expression of CD13 was not statistically different with control group (Fig. 5A, G, H). In the TBHP + bFGF group, the N-cadherin expression level was significantly higher than that of the TBHP group, but the fluorescence intensity of CD13$^+$ pericytes was not significantly different (Fig. 5F, G, H). Then the proportion of N-cadherin$^+$ & CD13$^+$ pericytes and the fluorescence intensity of N-cadherin were analyzed. It was shown that the N-cadherin mean immunofluorescence intensity in N-cadherin$^+$ & CD13$^+$ pericytes and the proportion of N-cadherin$^+$ & CD13$^+$ pericytes in the TBHP group were significantly down-regulated when compared with the control group (Fig. 5A, J). In the TBHP + bFGF group, the N-cadherin mean immunofluorescence intensity in N-cadherin$^+$ & CD13$^+$ pericytes and the proportion of N-cadherin$^+$ & CD13$^+$ pericytes were up-regulated when compared with the TBHP group (Fig. 5A, J). In the bFGF group, the N-cadherin mean immunofluorescence intensity in N-cadherin$^+$ & CD13$^+$ pericytes was up-regulated but the proportion of N-cadherin$^+$ &

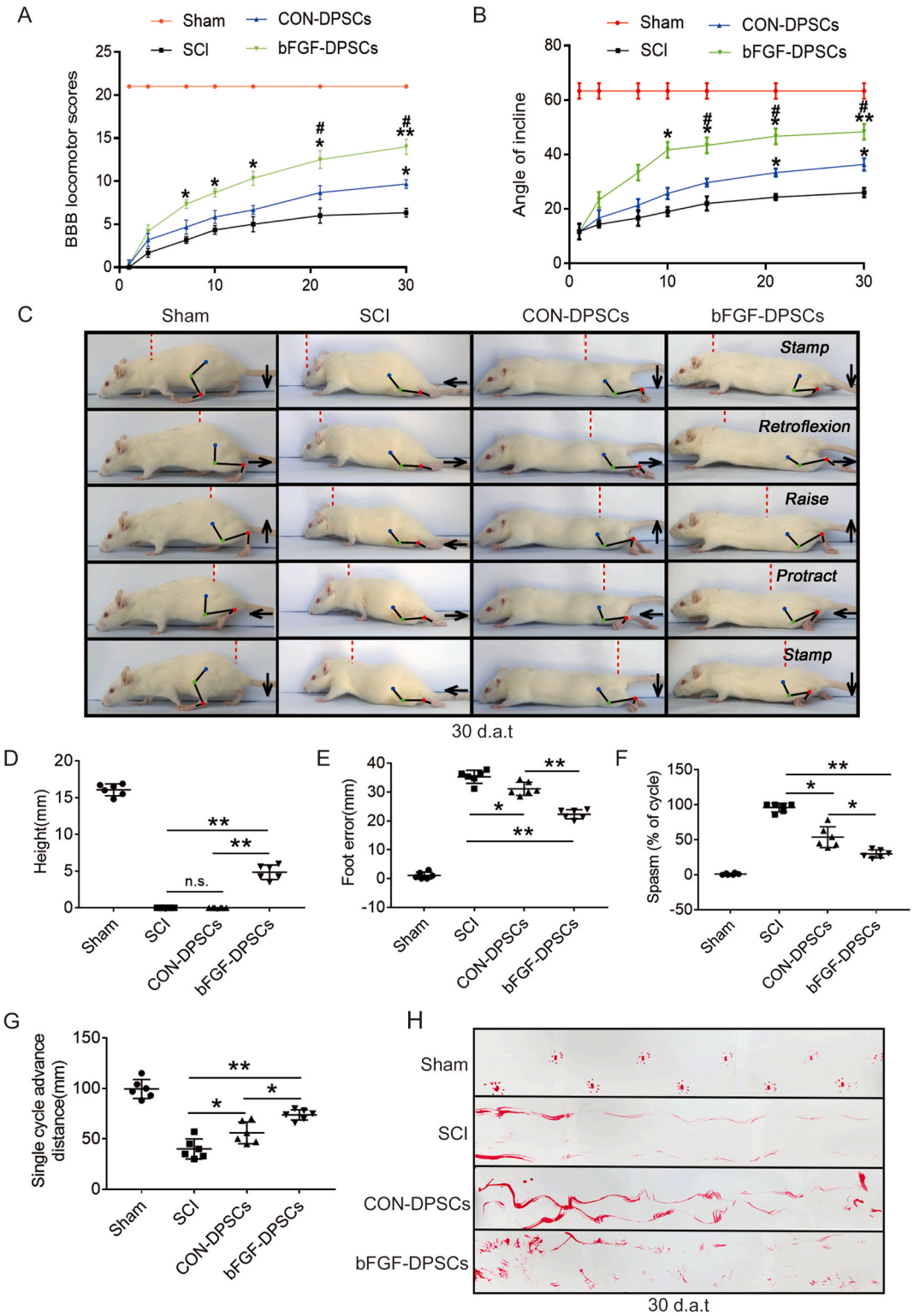

Fig. 8. AAV-5HRE-bFGF-DPSCs promote the recovery of locomotion in SCI rats. **(A)** The BBB scores of the rats in the Sham, SCI group, AAV-5HRE-DPSCs (CON-DPSCs) group and AAV-5HRE-bFGF-DPSCs (bFGF-DPSCs) group. **(B)** The inclined plane test scores of rats in the Sham, SCI group, CON-DPSCs group and bFGF-DPSCs group. **(C)** Video sequences showing rats walk in 30 d.a.t. Accordingly, the weight support, leg extensor spasms, slow steps and foot placement were analyzed. Foot movement is highlighted by arrows. The initial position of the move is highlighted by red dots. Scale bar: 20 mm. **(D)** Weight support (quantified as the height of the trunk from the ground). **(E)** Foot error. **(F)** Spasm. **(G)** Single cycle advance distance. **(H)** Footprint analysis of Sham, SCI group, CON-DPSCs group and bFGF-DPSCs group in 30 d.a.t.. * represents $P < 0.05$. ** represents $P < 0.01$. *** represents $P < 0.001$. n.s. means no statistical significance. Data are represented as mean ± SD ($n = 6$). (For interpretation of the references to colour in this figure legend, the reader is referred to the Web version of this article.)

$CD13^+$ pericytes was not statistically different with the control group (Fig. 5F, I, J). These results further demonstrated that bFGF up-regulates N-cadherin level in $CD13^+$ pericytes under normal or damaging conditions but could not protect it from damage.

To further evaluate the roles of bFGF in regulating N-cadherin in $CD13^+$ pericytes, Western blot was performed in different drug-treated groups. Consistent with the previous results, Western blot revealed that N-cadherin of the TBHP group and TBHP + bFGF group decreased when compared with the control group, while N-cadherin of the bFGF group increased when compared with the control group. The N-cadherin expression level of TBHP + bFGF group was significantly lower than that of the TBHP group (Fig. S4A, B). Subsequently, the expression of N-cadherin 30 d.a.t. was investigated by Western blot, revealing an opposite trend of N-cadherin expression (Fig. S4C, D). Indicated by immunofluorescence staining, N-cadherin was also expressed in astrocytes in addition to $CD13^+$ pericytes and the cell numbers of N-$cadherin^+$ & $GFAP^+$ cells in each group were in a similar pattern when compared to the Western blot results shown above (Fig. S4E, F). Studies have reported that the N-cadherin expression in astrocytes after SCI is up-regulated by the increased c Jun N terminal kinase 1 (JNK1) [36]. Here the expression of N-cadherin in astrocytes was studied. It was indicated by Western blot that, N-cadherin increased in the TBHP and TBHP + bFGF groups and N-cadherin decreased in the bFGF group when compared with the control group. N-cadherin of the TBHP + bFGF group was significantly lower than that of the TBHP group (Fig. S4G, H). This result was consistent with our above conclusion.

$CD13^+$ pericytes promote the recovery of hypoxic microenvironment in SCI via regulating microvascular diameter.

To explore the roles of $CD13^+$ pericytes in regulating hypoxia microenvironment, CD31 and CD13 were co-stained. The microvascular diameter of SCI rats was revealed to be significantly larger than that of the Sham group rats, accompanied with CD13 deficiency. Although the number of $CD13^+$ pericytes increased in the CON-DPSCs group, the change of the microvascular diameter was limited. In the bFGF-DPSCs group, the diameter of the capillaries was significantly decreased (Fig. 6A, E). Intriguingly, most of the $CD13^+$ pericytes in the bFGF group was attached to vascular endothelial cells after SCI, and $CD13^+$ pericytes attachment was present in the constriction place of vascular endothelial cells. The microvascular diameter changed significantly before and after the vasoconstriction point (Fig. 6A, F). Then the mechanism by which $CD13^+$ pericytes promoted vasoconstriction was investigated. It was indicated that dopa decarboxylase (DDC) in $CD13^+$ pericytes was activated, and 5HT was generated after SCI (Fig. 6B, C, G, H). The 5-HT produced by $CD13^+$ pericytes acted on its own 5HT-1B, which constricted microvessels (Fig. 6D, I). Generally, $CD13^+$ pericytes constrict microvascular via the DDC-5HT-5HT-1B pathway when they attach to vascular endothelial cells.

AAV-5HRE-bFGF-DPSCs promote the overall recovery of SCI by inhibiting energy-related autophagy.

The survived neurons after SCI plays an important role in the recovery of motor function. NeuN and GAP43 were used to label the regenerated neurons and growing axons. The numbers of neurons and axons in the bFGF-DPSCs group were significantly higher than those in the SCI group and CON-DPSCs group, indicating that AAV-5HRE-bFGF-DPSCs promoted the survival of neurons and axon regeneration (Fig. 7A–C). Indicated by full-image analysis of the spinal cord and Nissl staining, we further found that AAV-5HRE-bFGF-DPSCs reduced the area of injury and promoted neuronal survival and axonal regeneration (Fig. S5). Most of neurons in the bFGF-DPSCs group were found to co-express bFGF (Fig. 7D–F), suggesting that bFGF-DPSCs not only differentiated into pericytes, but also differentiated into neurons. Autophagy is known as one of the programmed cell death modes that regulates cell death [37,38]. Among autophagy pathways, AMPK-mTOR-ULK1 pathway is most closely related to energy metabolism [39–41]. Due to the hypoxia microenvironment caused by SCI, the energy metabolism of cells are significantly affected [42,43]. Thus, we hypothesized that the survival of neurons was regulated by AMPK-mTOR-ULk1 pathway. LC3 II, ULK1 and P62 in the spinal cord and neurons were immunostained, showing that the fluorescence intensity of LC3 II, ULK1 and P62 in the bFGF-DPSCs group was significantly lower than that of the SCI group and CON-DPSCs group. Especially, the autophagy in neurons was significantly inhibited. Subsequently, AMPK-1α, mTOR, ULK1 and LC3 were investigated using Western blot to verify the inhibition of AMPK-mTOR-ULK1 autophagy pathway (Fig. S6). It was revealed that AAV-5HRE-bFGF-DPSCs inhibited AMPK-mTOR-ULK1 autophagy pathway to promote neuronal survival and further improved the hypoxia microenvironment. After that, the ability of regenerated axons to pass through glial scars was also investigated. GFAP and Laminin were immunostained and shown to significantly decrease in the bFGF-DPSCs group when compared with the SCI group and CON-DPSCs group (Fig. S7A-C). These results indicated that both glial and fibrous scars were inhibited. After that, the axons were labeled with NF200. It was shown that the axons in the bFGF-DPSCs group passed through the glial scar, and the diameter of the axons were close to the normal level, which greatly promoted the recovery of spinal cord injury. In addition, the axonal growth suppression-related protein Neurocan was revealed to be inhibited (Fig. S7D-J).

3.5. *AAV-5HRE-bFGF-DPSCs improve motor function recovery of SCI rats*

Functional recovery was evaluated 1, 3, 7, 10, 14, 21 and 30 d.a.t.. It was revealed by BBB scales results that the bFGF-DPSCs group scored higher than the CON-DPSCs group and SCI group (Fig. 8A). Consistently, rats in bFGF-DPSCs group climbed a higher angle than the rats in the CON-DPSCs group and SCI group (Fig. 8B). In addition, the hindlimb movement ability of rats in each group were recorded and evaluated. As expected, in the SCI group, the connection lines of hindlimb joints were approximately horizontal and straight, and there was no obvious joint movement in lower limb paralysis. In the CON-DPSCs group, the hind limb joints of the rats were able to move but not strong enough to support their weight. In contrast, rats in the bFGF-DPSCs group were able to continuously support the body weight, and some of them were able to move the front and rear limbs together frequently (Fig. 8C). Quantitative analysis revealed that the rats in the bFGF-DPSCs group had higher maximum height from the ground (Fig. 8D), more effective plantar support range (Fig. 8E), shorter spasm duration (Fig. 8F) and greater forward distance for a single hind leg cycle (Fig. 8G) than the rats in the CON-DPSCs group and SCI group, which was an indication of improved of hindlimb motor function after the transplantation of AAV-5HRE-bFGF-DPSCs in SCI rats. Furthermore, in the footstep imprinting experiment, rats in the sham group showed clear imprinting, orderly arrangement and along the same straight line. Rats in the SCI group and CON-DPSCs group showed severe imprinting disorder with a wave shape and dragged movement. However, in the bFGF-DPSCs group, although the imprinting was disordered, the off-ground movement of hind limbs could be clearly observed (Fig. 8H). Collectively, it was indicated by these results that rats in bFGF-DPSCs group had improved motor functional recovery when compared with rats in CON-DPSCs group and SCI group.

4. Discussion

SCI is a common disease in the central nervous system [44,45]. Currently, researches on protection and regeneration of neurons, especially the self-regeneration of neurons have been widely performed [46,47]. However, little is known about the regulation of the microenvironment in SCI. After SCI, an ischemia and hypoxia environment, unsuitable for cell living, is induced because of vascular rupture [48,49]. Studies have shown that vascular endothelial cells are not lacked in the chronic convalescence of SCI [50]. However, we found that the hypoxia microenvironment in the damage area of chronic convalescence spinal

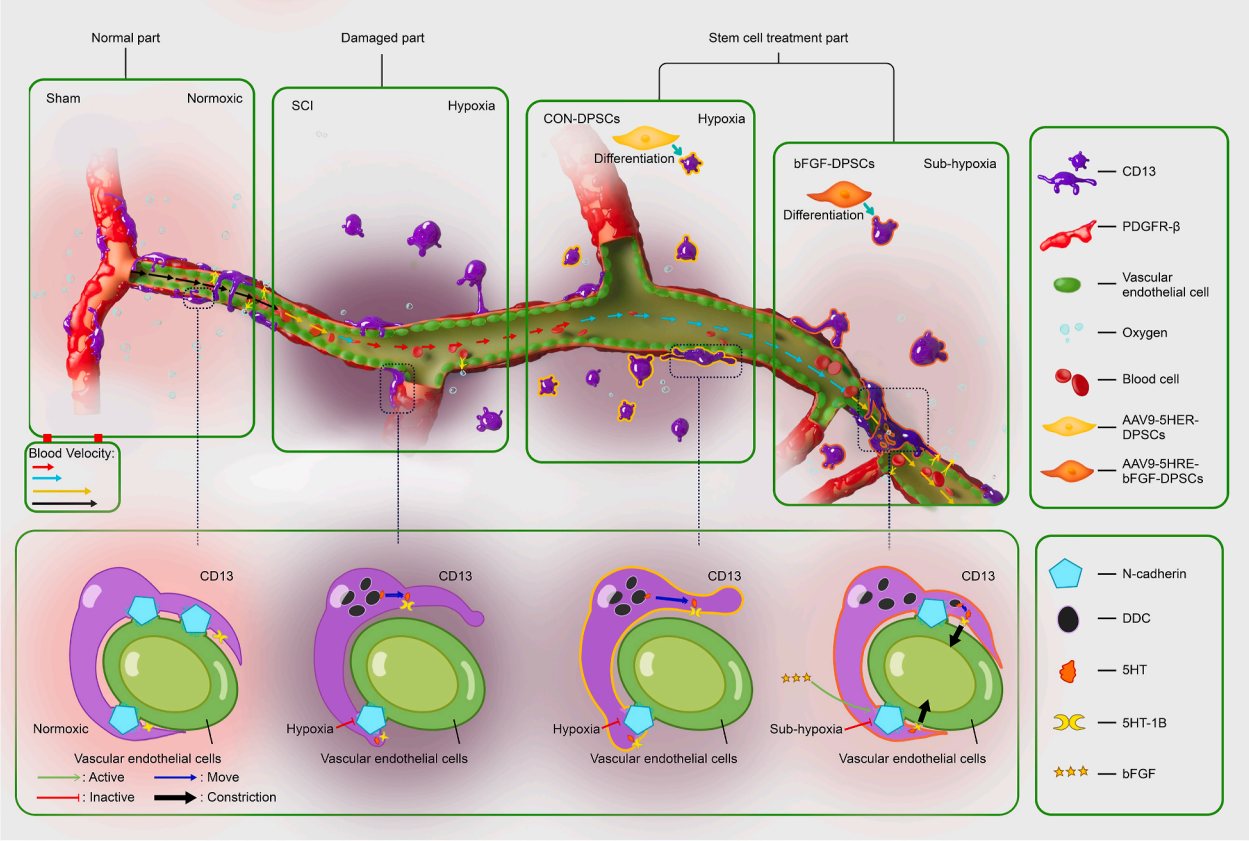

Fig. 9. AAV-5HRE-bFGF-DPSCs significantly improve the hypoxia microenvironment after SCI by differentiating into $CD13^+$ pericytes and up-regulating N-cadherin to promote $CD13^+$ pericytes' regulation of vascular diameter.

cord was not alleviated (Fig. 2). Therefore, we focused on the perivascular cells to find the key targets to improve the hypoxic microenvironment in the spinal cord.

First, PDGFR-β^+ pericytes were examined. PDGFR-β^+ pericytes have been reported to regulate vascular permeability in stroke and other diseases [51,52], which may also be able to regulate the hypoxia microenvironment. However, in our study, we found that PDGFR-β^+ pericytes expressed the same proliferation trend as vascular endothelial cells after SCI without significant changes in vascular coverage (Fig. S2). Studies have reported that PDGFR-β^+ pericytes are closely related to the formation of fibrous scar [53–55]. Thus, we turned to other types of pericytes, $CD13^+$ pericytes. $CD13^+$ pericytes have been shown to involve in constricting blood vessels, regulating blood flow and promoting angiogenesis [56–58]. In our study, it was demonstrated that $CD13^+$ pericytes activate DCC to produce 5-HT after SCI. Then, 5-HT binds with 5HT-1B carried by $CD13^+$ pericytes and produces contractile effects (Fig. 6). During this process, the contractile effects are significantly limited because of two reasons: (1). Large number of $CD13^+$ pericytes die after SCI, (2). Survived $CD13^+$ pericytes in the injured spinal cord appear to be unable to attach to vascular endothelial cells.

DPSCs are mesenchymal stem cells with the ability to differentiate into various cells [23,25,59] including neurons and vascular cells [60,61]. In our study, we observed that DPSCs differentiated into $CD13^+$ pericytes *in vitro* and *in vivo* and differentiated into neurons *in vivo* (Figs. 5 and 7), which provided a complement to the loss of $CD13^+$ pericytes and neurons in SCI. bFGF has been known as an excellent nerve growth factor with neuroprotective effects [62–64]. Here, in our study we demonstrated the role of bFGF in promoting the expression of N-cadherin in $CD13^+$ pericytes in rat SCI model (Fig. 5; Fig. S4). Since the excessive dose of bFGF can lead to gliomas formation, a controlled combination administration of bFGF and DPSC is urgently needed. The use of AAV in neuroscience is popular these days. Compared with lentivirus and adenovirus, AAV has more stable expression and lower immune rejection. In our research, DPSCs were transfected with AAV-5HRE-bFGF and successfully expressed bFGF only in hypoxic environment *in vivo* and *in vitro* (Figs. 1 and 2). The effects of this AAV-5HRE-bFGF-DPSCs system may not be as good as bFGF overexpressed genes. However, since AAV-5HRE-bFGF-DPSCs is regulated by hypoxia, the bFGF expression will be stopped when the hypoxic microenvironment induced by SCI returns to normoxic environment. This system greatly reduces the risk of neuroma induction and lays a solid foundation for clinical transformation in the future.

Administration of AAV-5HRE-bFGF-DPSCs made a compensation of the loss of $CD13^+$ pericytes after SCI. AAV-5HRE-bFGF-DPSCs differentiated into $CD13^+$ pericytes and secreted bFGF to up-regulate the N-cadherin expression, promoting the adhesion of $CD13^+$ pericytes to vascular endothelial cells and inducing vasoconstriction (Figs. 4 and 5). After that, the hypoxic microenvironment induced by SCI was greatly improved (Fig. S2). We found that the microvessel diameter of SCI group was doubled or even tripled when compared with the control group. According to the flow rate calculation formula in the ideal state: V (flow velocity) = Q (quantity of flow)/S (microvascular cross-sectional area), blood flow velocity of SCI rats is 1/4 or even 1/9 of normal. The decreased blood flow velocity greatly reduces the efficiency of internal and external exchange between oxygen and carbon dioxide. In addition, the hypoxia in the damaged area is further aggravated because of the high metabolism during the repair and regeneration process (Fig. 6). The improvement of diameter regulated by $CD13^+$ pericytes was clearly observed in the bFGF-DPSCs group. The diameter of microvessels in bFGF-DPSCs group is significantly smaller than that in SCI group, and the diameter distribution range of microvessels is the largest among the

four groups (Fig. 6E). To further verify if the hypoxic microenvironment was improved, AMPK-mTOR-ULK1 autophagy pathway associated with energy metabolism was investigated. Researches have demonstrated that thirty days after SCI, the programmed cell death pathways which play major roles in acute stage, including endoplasmic reticulum stress-related pathways, ATG5-LC3 pathway and Beclin 1-VPS-34 complex pathway were no longer obvious [48,61,65–67]. In our experiment, we found that AMPK-mTOR-ULK1 autophagy pathway was inhibited, indicating the improved hypoxia microenvironment in the SCI rats (Fig. 7). Subsequently, the motor function of rats was also improved (Fig. 8).

In conclusion, AAV-5HRE-bFGF-DPSCs can improve SCI recovery via two mechanisms. (1). AAV-5HRE-bFGF-DPSCs ameliorate the SCI-induced hypoxia microenvironment via differentiating into $CD13^{+}$ pericytes and up-regulating N-cadherin to promote $CD13^{+}$ pericytes' regulation of vascular diameter. (2). AAV-5HRE-bFGF-DPSCs differentiate into neurons, promoting the overall recovery of SCI (Fig. 9).

Acknowledgments

This study was partly funded by a grant the National Natural Science Foundation of China (81802235, 81871503), Zhejiang Medical and Health Science and Technology Plan Project (2021KY212), and Wenzhou Basic Science Research Plan Project (Y2020050), Advanced Postdoctoral Programs of Zhejiang (zj2019030), China Postdoctoral Science Foundation (2019M662015), CAMS Innovation Fund for Medical Sciences (2019-I2M-5-028).

Appendix A. Supplementary data

Supplementary data to this article can be found online at https://doi.org/10.1016/j.bioactmat.2021.01.024.

Author contribution

Sipin Zhu and Yibo Ying coordinated and carried out most of the experiments and data analysis and participated in drafting the manuscript. Yan He, Xingxing Zhong, Jiahui Ye, Ziyang Huang, Min Chen and Qiuji Wu provided technical assistance. Yifan Zhang, Yan He, Ziyue Xiang, Yurong Tu and Weiyang Ying carried out assistance on data analysis and manuscript preparation. Sipin Zhu supervised the project and experimental designs and data analysis. Jian Xiao revised the manuscript. Zhouguang Wang, Xiaokun Li and Qingsong Ye supervised the project and revised the manuscript. All authors approved the final manuscript.

Data availability statement

The data used to support the findings of this study are available from the corresponding authors upon request.

Conflicts of interest

All authors declare no conflict of interest.

References

[1] P. Assinck, G. Duncan, B. Hilton, J. Plemel, W. Tetzlaff, Cell transplantation therapy for spinal cord injury, Nat. Neurosci. 20 (2017) 637–647, https://doi.org/10.1038/nn.4541.
[2] G. Courtine, M. Sofroniew, Spinal cord repair: advances in biology and technology, Nat. Med. 25 (2019) 898–908, https://doi.org/10.1038/s41591-019-0475-6.
[3] A. Domínguez-Bajo, A. González-Mayorga, C. Guerrero, F. Palomares, R. García, E. López-Dolado, M. Serrano, Myelinated axons and functional blood vessels populate mechanically compliant rGO foams in chronic cervical hemisected rats, Biomaterials 192 (2019) 461–474, https://doi.org/10.1016/j.biomaterials.2018.11.024.
[4] S. Halder, R. Kant, R. Milner, Chronic mild hypoxia promotes profound vascular remodeling in spinal cord blood vessels, preferentially in white matter, via an α5β1 integrin-mediated mechanism, Angiogenesis 21 (2018) 251–266, https://doi.org/10.1007/s10456-017-9593-2.
[5] J. Lee, H. Choi, T. Yune, MMP-3 secreted from endothelial cells of blood vessels after spinal cord injury activates microglia, leading to oligodendrocyte cell death, Neurobiol. Dis. 82 (2015) 141–151, https://doi.org/10.1016/j.nbd.2015.06.002.
[6] M. Perdiki, M. Farooque, A. Holtz, G. Li, Y. Olsson, Expression of endothelial barrier antigen immunoreactivity in blood vessels following compression trauma to rat spinal cord. Temporal evolution and relation to the degree of the impact, Acta Neuropathol. 96 (1998) 8–12, https://doi.org/10.1007/s004010050854.
[7] M. Ng, A. Stammers, B. Kwon, Vascular disruption and the role of angiogenic proteins after spinal cord injury, Translational stroke research 2 (2011) 474–491, https://doi.org/10.1007/s12975-011-0109-x.
[8] C. Ahuja, J. Wilson, S. Nori, M. Kotter, C. Druschel, A. Curt, M. Fehlings, Traumatic spinal cord injury, Nature reviews. Disease primers. 3 (2017) 17018, https://doi.org/10.1038/nrdp.2017.18.
[9] S. Guo, I. Redenski, S. Landau, A. Szklanny, U. Merdler, S. Levenberg, Prevascularized scaffolds bearing human dental pulp stem cells for treating complete spinal cord injury, Advanced healthcare materials 9 (2020), e2000974, https://doi.org/10.1002/adhm.202000974.
[10] W. Whetstone, J. Hsu, M. Eisenberg, Z. Werb, L. Noble-Haeusslein, Blood-spinal cord barrier after spinal cord injury: relation to revascularization and wound healing, J. Neurosci. Res. 74 (2003) 227–239, https://doi.org/10.1002/jnr.10759.
[11] F. Xiao, Y. Guo, J. Deng, F. Yuan, Y. Xiao, L. Hui, Y. Li, Z. Hu, Y. Zhou, K. Li, X. Han, Q. Fang, W. Jia, Y. Chen, H. Ying, Q. Zhai, S. Chen, F. Guo, Hepatic c-Jun regulates glucose metabolism via FGF21 and modulates body temperature through the neural signals, Molecular metabolism 20 (2019) 138–148, https://doi.org/10.1016/j.molmet.2018.12.003.
[12] Y. Li, A. Lucas-Osma, S. Black, M. Bandet, M. Stephens, R. Vavrek, L. Sanelli, K. Fenrich, A. Di Narzo, S. Dracheva, I. Winship, K. Fouad, D. Bennett, Pericytes impair capillary blood flow and motor function after chronic spinal cord injury, Nat. Med. 23 (2017) 733–741, https://doi.org/10.1038/nm.4331.
[13] S. Zhu, M. Chen, L. Deng, J. Zhang, W. Ni, X. Wang, F. Yao, X. Li, H. Xu, J. Xu, J. Xiao, The repair and autophagy mechanisms of hypoxia-regulated bFGF-modified primary embryonic neural stem cells in spinal cord injury, Stem cells translational medicine 9 (2020) 603–619, https://doi.org/10.1002/sctm.19-0282.
[14] W. Liu, Y. Rong, J. Wang, Z. Zhou, X. Ge, C. Ji, D. Jiang, F. Gong, L. Li, J. Chen, S. Zhao, F. Kong, C. Gu, J. Fan, W. Cai, Exosome-shuttled miR-216a-5p from hypoxic preconditioned mesenchymal stem cells repair traumatic spinal cord injury by shifting microglial M1/M2 polarization, J. Neuroinflammation 17 (2020) 47, https://doi.org/10.1186/s12974-020-1726-7.
[15] H. Zhang, D. Li, Y. Zhang, J. Li, S. Ma, J. Zhang, Y. Xiong, W. Wang, N. Li, L. Xia, Knockdown of lncRNA BDNF-AS suppresses neuronal cell apoptosis via downregulating miR-130b-5p target gene PRDM5 in acute spinal cord injury, RNA Biol. 15 (2018) 1071–1080, https://doi.org/10.1080/15476286.2018.1493333.
[16] T. Hutson, S. Di Giovanni, The translational landscape in spinal cord injury: focus on neuroplasticity and regeneration, Nat. Rev. Neurol. 15 (2019) 732–745, https://doi.org/10.1038/s41582-019-0280-3.
[17] A. Tran, P. Warren, J. Silver, The biology of regeneration failure and success after spinal cord injury, Physiol. Rev. 98 (2018) 881–917, https://doi.org/10.1152/physrev.00017.2017.
[18] H. Lee, H. Lee, B. Lee, D. Gerovska, S. Park, H. Zaehres, M. Araúzo-Bravo, J. Kim, Y. Ha, H. Schöler, J. Kim, Sequentially induced motor neurons from human fibroblasts facilitate locomotor recovery in a rodent spinal cord injury model, eLife 9 (2020), https://doi.org/10.7554/eLife.52069.
[19] S. Ceto, K. Sekiguchi, Y. Takashima, A. Nimmerjahn, M. Tuszynski, Neural stem cell grafts form extensive synaptic networks that integrate with host circuits after spinal cord injury, Cell stem cell 27 (2020) 430–440, https://doi.org/10.1016/j.stem.2020.07.007, e5.
[20] L. Liau, Q. Looi, W. Chia, T. Subramaniam, M. Ng, J. Law, Treatment of spinal cord injury with mesenchymal stem cells, Cell Biosci. 10 (2020) 112, https://doi.org/10.1186/s13578-020-00475-3.
[21] L. Luo, A. Albashari, X. Wang, L. Jin, Y. Zhang, L. Zheng, J. Xia, H. Xu, Y. Zhao, J. Xiao, Y. He, Q. Ye, Effects of transplanted heparin-poloxamer hydrogel combining dental pulp stem cells and bFGF on spinal cord injury repair, Stem Cell. Int. (2018) 2398521, https://doi.org/10.1155/2018/2398521.
[22] A. Albashari, Y. He, Y. Zhang, J. Ali, F. Lin, Z. Zheng, K. Zhang, Y. Cao, C. Xu, L. Luo, J. Wang, Q. Ye, Thermosensitive bFGF-modified hydrogel with dental pulp stem cells on neuroinflammation of spinal cord injury, ACS Omega 5 (2020) 16064–16075, https://doi.org/10.1021/acsomega.0c01379.
[23] X. Shi, J. Mao, Y. Liu, Pulp stem cells derived from human permanent and deciduous teeth: biological characteristics and therapeutic applications, Stem cells translational medicine 9 (2020) 445–464, https://doi.org/10.1002/sctm.19-0398.
[24] D. Wang, Y. Wang, W. Tian, J. Pan, Advances of tooth-derived stem cells in neural diseases treatments and nerve tissue regeneration, Cell Prolif 52 (2019), e12572, https://doi.org/10.1111/cpr.12572.
[25] X. Yang, L. Li, L. Xiao, D. Zhang, Recycle the dental fairy's package: overview of dental pulp stem cells, Stem Cell Res. Ther. 9 (2018) 347, https://doi.org/10.1186/s13287-018-1094-8.
[26] C. Yang, X. Li, L. Sun, W. Guo, W. Tian, Potential of human dental stem cells in repairing the complete transection of rat spinal cord, J. Neural. Eng. 14 (2017), 026005, https://doi.org/10.1088/1741-2552/aa596b.
[27] A. Yamamoto, K. Sakai, K. Matsubara, F. Kano, M. Ueda, Multifaceted neuro-regenerative activities of human dental pulp stem cells for functional recovery after

spinal cord injury, Neurosci. Res. 78 (2014) 16–20, https://doi.org/10.1016/j.neures.2013.10.010.
[28] M. Rathbone, P. Middlemiss, J. Gysbers, C. Andrew, M. Herman, J. Reed, R. Ciccarelli, P. Di Iorio, F. Caciagli, Trophic effects of purines in neurons and glial cells, Prog. Neurobiol. 59 (1999) 663–690, https://doi.org/10.1016/s0301-0082(99)00017-9.
[29] K. Abe, H. Saito, Effects of basic fibroblast growth factor on central nervous system functions, Pharmacol. Res. 43 (2001) 307–312, https://doi.org/10.1006/phrs.2000.0794.
[30] D. Sun, W. Wang, X. Wang, Y. Wang, X. Xu, F. Ping, Y. Du, W. Jiang, D. Cui, bFGF plays a neuroprotective role by suppressing excessive autophagy and apoptosis after transient global cerebral ischemia in rats, Cell Death Dis. 9 (2018) 172, https://doi.org/10.1038/s41419-017-0229-7.
[31] C. Ahuja, A. Mothe, M. Khazaei, J. Badhiwala, E. Gilbert, D. van der Kooy, C. Morshead, C. Tator, M. Fehlings, The leading edge: emerging neuroprotective and neuroregenerative cell-based therapies for spinal cord injury, Stem cells translational medicine 9 (2020) 1509–1530, https://doi.org/10.1002/sctm.19-0135.
[32] K. Bucher, E. Rodríguez-Bocanegra, D. Dauletbekov, M. Fischer, Immune responses to retinal gene therapy using adeno-associated viral vectors - implications for treatment success and safety, Prog. Retin. Eye Res. (2020) 100915, https://doi.org/10.1016/j.preteyeres.2020.100915.
[33] M. Lugin, R. Lee, Y. Kwon, Synthetically engineered adeno-associated virus for efficient, safe, and versatile gene therapy applications, ACS Nano 14 (2020) 14262–14283, https://doi.org/10.1021/acsnano.0c03850.
[34] M. Wang, H. Xu, Y. Li, C. Cao, H. Zhu, Y. Wang, Z. Zhao, G. Pei, F. Zhu, Q. Yang, X. Deng, C. Zhou, Y. Guo, J. Wu, W. Liao, J. Yang, Y. Yao, R. Zeng, Exogenous bone marrow derived-putative endothelial progenitor cells attenuate ischemia reperfusion-induced vascular injury and renal fibrosis in mice dependent on pericytes, Theranostics 10 (2020) 12144–12157, https://doi.org/10.7150/thno.48562.
[35] E. Watanabe, T. Wada, A. Okekawa, F. Kitamura, G. Komatsu, Y. Onogi, S. Yamamoto, M. Sasahara, M. Kitada, D. Koya, H. Tsuneki, T. Sasaoka, Stromal cell-derived factor 1 (SDF1) attenuates platelet-derived growth factor-B (PDGF-B)-induced vascular remodeling for adipose tissue expansion in obesity, Angiogenesis 23 (2020) 667–684, https://doi.org/10.1007/s10456-020-09738-6.
[36] C. Jo, Y. Koh, Cadmium induces N-cadherin cleavage via ERK-mediated γ-secretase activation in C6 astroglia cells, Toxicol. Lett. 222 (2013) 117–121, https://doi.org/10.1016/j.toxlet.2013.07.015.
[37] J. Doherty, E. Baehrecke, Life, death and autophagy, Nat. Cell Biol. 20 (2018) 1110–1117, https://doi.org/10.1038/s41556-018-0201-5.
[38] N. Mizushima, A brief history of autophagy from cell biology to physiology and disease, Nat. Cell Biol. 20 (2018) 521–527, https://doi.org/10.1038/s41556-018-0092-5.
[39] C. Johnson, A. Tee, Exploiting cancer vulnerabilities: mTOR, autophagy, and homeostatic imbalance, Essays Biochem. 61 (2017) 699–710, https://doi.org/10.1042/ebc20170056.
[40] E. Dunlop, A. Tee, mTOR and autophagy: a dynamic relationship governed by nutrients and energy, Semin. Cell Dev. Biol. 36 (2014) 121–129, https://doi.org/10.1016/j.semcdb.2014.08.006.
[41] F. Din, A. Valanciute, V. Houde, D. Zibrova, K. Green, K. Sakamoto, D. Alessi, M. Dunlop, Aspirin inhibits mTOR signaling, activates AMP-activated protein kinase, and induces autophagy in colorectal cancer cells, Gastroenterology 142 (2012) 1504–1515, https://doi.org/10.1053/j.gastro.2012.02.050, e3.
[42] R. Desai, A. Davies, M. Tachrount, M. Kasti, F. Laulund, X. Golay, K. Smith, Cause and prevention of demyelination in a model multiple sclerosis lesion, Ann. Neurol. 79 (2016) 591–604, https://doi.org/10.1002/ana.24607.
[43] A. Davies, R. Desai, P. Bloomfield, P. McIntosh, K. Chapple, C. Linington, R. Fairless, R. Diem, M. Kasti, M. Murphy, K. Smith, Neurological deficits caused by tissue hypoxia in neuroinflammatory disease, Ann. Neurol. 74 (2013) 815–825, https://doi.org/10.1002/ana.24006.
[44] J. McDonald, C. Sadowsky, Spinal-cord injury, Lancet (London, England) 359 (2002) 417–425, https://doi.org/10.1016/s0140-6736(02)07603-1.
[45] Y. Song, N. Agrawal, J. Griffin, C. Schmidt, Recent advances in nanotherapeutic strategies for spinal cord injury repair, Adv. Drug Deliv. Rev. 148 (2019) 38–59, https://doi.org/10.1016/j.addr.2018.12.011.
[46] V. Dietz, A. Curt, Neurological aspects of spinal-cord repair: promises and challenges, Lancent, Neurol. 5 (2006) 688–694, https://doi.org/10.1016/s1474-4422(06)70522-1.
[47] A. Blight, Miracles and molecules–progress in spinal cord repair, Nat. Neurosci. (2002) 1051–1054, https://doi.org/10.1038/nn939.
[48] C. Ahuja, M. Fehlings, Concise review: bridging the gap: novel neuroregenerative and neuroprotective strategies in spinal cord injury, Stem cells translational medicine 5 (2016) 914–924, https://doi.org/10.5966/sctm.2015-0381.
[49] M. McEwen, P. Sullivan, A. Rabchevsky, J. Springer, Targeting mitochondrial function for the treatment of acute spinal cord injury, Neurotherapeutics : the journal of the American Society for Experimental NeuroTherapeutics. 8 (2011) 168–179, https://doi.org/10.1007/s13311-011-0031-7.
[50] T. Zhou, Y. Zheng, L. Sun, S. Badea, Y. Jin, Y. Liu, A. Rolfe, H. Sun, X. Wang, Z. Cheng, Z. Huang, N. Zhao, X. Sun, J. Li, J. Fan, C. Lee, T. Megraw, W. Wu, G. Wang, Y. Ren, Microvascular endothelial cells engulf myelin debris and promote macrophage recruitment and fibrosis after neural injury, Nat. Neurosci. 22 (2019) 421–435, https://doi.org/10.1038/s41593-018-0324-9.
[51] K. Gertz, G. Kronenberg, R. Uhlemann, V. Prinz, R. Marquina, M. Corada, E. Dejana, M. Endres, Partial loss of VE-cadherin improves long-term outcome and cerebral blood flow after transient brain ischemia in mice, BMC Neurol. 16 (2016) 144, https://doi.org/10.1186/s12883-016-0670-8.
[52] S. Bhowmick, V. D'Mello, D. Caruso, A. Wallerstein, P. Abdul-Muneer, Impairment of pericyte-endothelium crosstalk leads to blood-brain barrier dysfunction following traumatic brain injury, Exp. Neurol. 317 (2019) 260–270, https://doi.org/10.1016/j.expneurol.2019.03.014.
[53] C. Reeves, A. Pradim-Jardim, S. Sisodiya, M. Thom, J. Liu, Spatiotemporal dynamics of PDGFRβ expression in pericytes and glial scar formation in penetrating brain injuries in adults, Neuropathol. Appl. Neurobiol. 45 (2019) 609–627, https://doi.org/10.1111/nan.12539.
[54] Y. Chen, F. Chang, C. Wu, Y. Chou, H. Hsu, W. Chiang, J. Shen, Y. Chen, K. Wu, T. Tsai, J. Duffield, S. Lin, Platelet-derived growth factor receptor signaling activates pericyte-myofibroblast transition in obstructive and post-ischemic kidney fibrosis, Kidney Int. 80 (2011) 1170–1181, https://doi.org/10.1038/ki.2011.208.
[55] J. Kyyriäinen, X. Ekolle Ndode-Ekane, A. Pitkänen, Dynamics of PDGFRβ expression in different cell types after brain injury, Glia 65 (2017) 322–341, https://doi.org/10.1002/glia.23094.
[56] E. Dondossola, R. Rangel, L. Guzman-Rojas, E. Barbu, H. Hosoya, L. St John, J. Molldrem, A. Corti, R. Sidman, W. Arap, R. Pasqualini, CD13-positive bone marrow-derived myeloid cells promote angiogenesis, tumor growth, and metastasis, Proc. Natl. Acad. Sci. U.S.A. 110 (2013) 20717–20722, https://doi.org/10.1073/pnas.1321139110.
[57] J. Sun, Y. Huang, J. Gong, J. Wang, Y. Fan, J. Cai, Y. Wang, Y. Qiu, Y. Wei, C. Xiong, J. Chen, B. Wang, Y. Ma, L. Huang, X. Chen, S. Zheng, W. Huang, Q. Ke, T. Wang, X. Li, W. Zhang, A. Xiang, W. Li, Transplantation of hPSC-derived pericyte-like cells promotes functional recovery in ischemic stroke mice, Nat. Commun. 11 (2020) 5196, https://doi.org/10.1038/s41467-020-19042-y.
[58] L. Xueyong, C. Shaozong, L. Wangzhou, L. Yuejun, L. Xiaoxing, L. Jing, W. Yanli, L. Jinqing, Differentiation of the pericyte in wound healing: the precursor, the process, and the role of the vascular endothelial cell, Wound repair and regeneration : official publication of the Wound Healing Society [and] the European Tissue Repair Society. http://doi.org/10.1111/j.1524-475X.2008.00374.x, 2008, 16, 346-355.
[59] K. Fawzy El-Sayed, R. Elsalawy, N. Ibrahim, M. Gadalla, H. Albargasy, N. Zahra, S. Mokhtar, N. El Nahhas, Y. El Kaliouby, C. Dörfer, The dental pulp stem/progenitor cells-mediated inflammatory-regenerative Axis, tissue engineering, Part B, Reviews. 25 (2019) 445–460, https://doi.org/10.1089/ten.TEB.2019.0106.
[60] D. Majumdar, M. Kanafi, R. Bhonde, P. Gupta, I. Datta, Differential neuronal plasticity of dental pulp stem cells from exfoliated deciduous and permanent teeth towards dopaminergic neurons, J. Cell. Physiol. 231 (2016) 2048–2063, https://doi.org/10.1002/jcp.25314.
[61] A. Arthur, G. Rychkov, S. Shi, S. Koblar, S. Gronthos, Adult human dental pulp stem cells differentiate toward functionally active neurons under appropriate environmental cues, Stem cells (Dayton, Ohio) 26 (2008) 1787–1795, https://doi.org/10.1634/stemcells.2007-0979.
[62] J. Ma, J. Qiu, L. Hirt, T. Dalkara, M. Moskowitz, Synergistic protective effect of caspase inhibitors and bFGF against brain injury induced by transient focal ischaemia, Br. J. Pharmacol. 133 (2001) 345–350, https://doi.org/10.1038/sj.bjp.0704075.
[63] Y. Zhao, M. Lin, Q. Lin, W. Yang, X. Yu, F. Tian, K. Mao, J. Yang, C. Lu, H. Wong, Intranasal delivery of bFGF with nanoliposomes enhances in vivo neuroprotection and neural injury recovery in a rodent stroke model, J. Contr. Release : official journal of the Controlled Release Society 224 (2016) 165–175, https://doi.org/10.1016/j.jconrel.2016.01.017.
[64] N. Rothwell, J. Relton, Involvement of cytokines in acute neurodegeneration in the CNS, Neurosci. Biobehav. Rev. 17 (1993) 217–227, https://doi.org/10.1016/s0149-7634(05)80152-6.
[65] M. Beattie, Inflammation and apoptosis: linked therapeutic targets in spinal cord injury, Trends Mol. Med. 10 (2004) 580–583, https://doi.org/10.1016/j.molmed.2004.10.006.
[66] V. Almeida, A. Paiva, I. Sena, A. Mintz, L. Magno, A. Birbrair, Pericytes make spinal cord breathless after injury, Neuroscientist : a review journal bringing neurobiology, neurology and psychiatry 24 (2018) 440–447, https://doi.org/10.1177/1073858417731522.
[67] S. Ohri, M. Maddie, Y. Zhao, M. Qiu, M. Hetman, S. Whittemore, Attenuating the endoplasmic reticulum stress response improves functional recovery after spinal cord injury, Glia 59 (2011) 1489–1502, https://doi.org/10.1002/glia.21191.